INVESTIGATION OF REFLECTARRAY DESIGN TECHNIQUES FOR 5.8 GHZ FRESNEL ZONE POWER BEAMING

A Dissertation
Presented to
The Academic Faculty

By

Evan Shi

In Partial Fulfillment
of the Requirements for the Degree
Master of Science in the
School of Engineering
Department of Electrical and Computer Engineering

Georgia Institute of Technology

May 2021

INVESTIGATION OF REFLECTARRAY DESIGN TECHNIQUES FOR 5.8 GHZ FRESNEL ZONE POWER BEAMING

Thesis committee:

Dr. Gregory Durgin
Electrical and Computer Engineering
Georgia Institute of Technology

Dr. Gordon Stüber
Electrical and Computer Engineering
Georgia Institute of Technology

Dr. Madhavan Swaminathan
Electrical and Computer Engineering
Georgia Institute of Technology

Date approved: April 30, 2021

ACKNOWLEDGMENTS

Thank you Mom and Dad for having my back and looking out for me. I truly appreciate the great personal sacrifices you have made to get me where I am today, and I hope that I make you proud. Thank you Naomi for putting up with a mostly absentee brother for the last few years. I promise we will hang out more in the future.

Thank you Sunny. You helped me get out of my head when it was overwhelming and believed in me more than anyone.

Thank you my friends in Atlanta, for living room KBBQ and hotpot, for general shenanigans, for being my respite and true bros. Thank you my friends elsewhere and back home, for keeping me company while I work and for the games.

Thank you Dr. Durgin for first helping me find my footing in research all the way back in 2016, and for the steady support since then. Knowing that you were always on my side has helped me tremendously.

Finally, thanks to the Space Solar Power Institute and the Georgia Tech Research Institute for their financial support of my graduate education to help me reach my goals.

TABLE OF CONTENTS

LIST OF TABLES

LIST OF FIGURES

SUMMARY

Large-scale wireless power transfer using microwaves is a promising technology for power transmission over distances unsuited for physical wire connections, such as between orbit and the Earth. Using large transmitting and receiving apertures, it is possible to focus microwave energy to achieve efficient transfer. This is accomplished by adjusting the phase distribution across the surface of the transmitting array such that it behaves like a Fresnel lens. One method of generating the desired phase distribution is through use of an active reflectarray, comprised of many discrete 2-dimensional unit cells with varying reflection coefficient phases. This thesis investigates the effect of changing the unit cell geometry from square to hexagonal, modifying the individual patch element geometry, and incident pilot signal design for the reflectarray.

CHAPTER 1

INTRODUCTION

Wireless power transfer (WPT) is a broad term encompassing many types of technologies used for powering devices via electromagnetic fields without the use of a physical connection. Close range WPT has been broadly commercialized through standards like Qi for mobile devices [1], and there is some interest in using WPT to charge electric vehicles, especially in the autonomous context[2]. However, long range WPT for applications such as powering airborne drones, grid-scale space solar power, and off-grid remote locations is still in early stages of development. Figure 1.1 shows a simplified system layout for WPT.

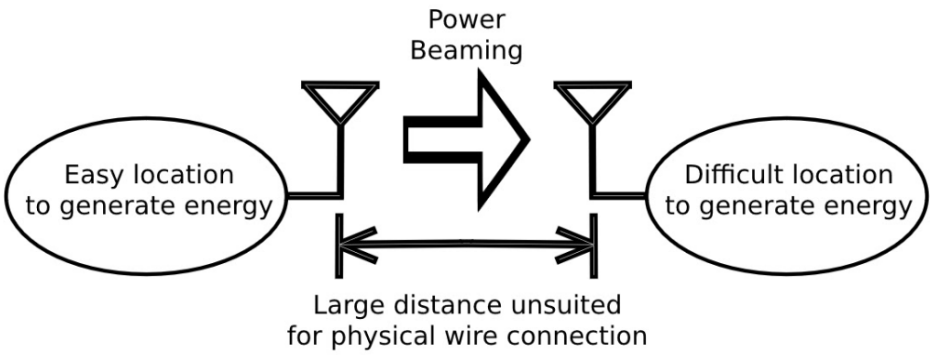

Figure 1.1: Simplified power beaming system overview.

Current research into long range WPT, also known as power beaming, can be broadly categorized into optical, mmWave, and microwave techniques based on the frequency of operation. Increasing the frequency through microwave into mmWave and optical regions presents different technical challenges within each frequency range. While a full examination of the merits of each frequency region is outside the scope of this work, a brief summary chart can be found in Table 1.1, reproduced from [3].

In exchange for low atmospheric attenuation and good conversion efficiency, microwave

Table 1.1: Comparison of power beaming carrier frequency regimes.

	Optical (300+ GHz)	mmWave (30-300 GHz)	Microwave (3-30 GHz)
Atmospheric penetration (clouds, rain, fog)	None	Low	High
Performance limits for DC to RF and RF to DC conversion efficiency	Medium	Medium	High
Required physical aperture size (both transmit and receive)	Small	Medium	Large
Safety (directivity, power density, public perception)	Low	Medium	Medium
Economy of scale	Low	Medium	High

power beaming requires large transmit and receive apertures for maximal transfer efficiency. While this is an issue from a cost perspective, safety limitations on power density in a practical system implementation most likely would have already mandated large transmit and receive apertures. In addition, increasing the aperture area of a microwave transmitter scales the transmitted power proportionally, which leads to greater economies of scale compared to mmWave and optical transmitters that have difficulties with continuous megawatt+ regime power (eg. high power lasers, mmWave amplifiers).

A key component of the overall system efficiency is the propagation efficiency over free space between the transmitter and receiver. This efficiency comprises atmospheric attenuation loss and the fraction of transmitted power that is "caught" by the receiver. Atmospheric attenuation loss in the microwave regime is small [4], so the dominating factor in propagation efficiency is the ability for a receiver to physically capture the majority of the transmitted energy. A rule of thumb proposed in [3] is:

"Beam collection efficiency exceeding 15% is only possible if the link distance is less than the far-field distance [5] of at least one of the two apertures."

The region closer to the transmitting aperture than the defined far-field distance and further than the reactive near-field distance is referred to as the Fresnel zone. Within this

zone, optimizing transmitter design using far-field assumptions to calculate far-field directivity and gain may not directly result in improved transfer efficiency. A Fresnel zone wireless link should be optimized instead by designing a "focus spot", modeled by a Gaussian beam [6]. In such a system, the amplitude and phase pattern across the transmitting aperture is designed such that the electric field intensity comes to a maximum on an area at some focal distance away from the transmit aperture. Modifying only the phase is sufficient to create a focal region, so more complex amplitude control is not required [7][8]. The mathematical expression for the phase ϕ across a circular aperture to produce a focus spot in the Fresnel zone is:

$$\phi(x, y) = \frac{2\pi}{\lambda}\left(\sqrt{x^2 + y^2 + F^2} - F\right) \tag{1.1}$$

where F is the distance from the aperture at which the focus spot is located.

A transmitter aperture phase distribution can be controlled by manipulating the physical path lengths between a source and the points on a reflector, as in a physical reflecting dish, by controlling the phase of separately transmitting elements, as in a phased array, or by varying the resonant frequency of the elements of a planar metasurface to control the phase of a reflected wave. This metasurface approach is the basis for what is known as a reflectarray antenna [9][10].

One potential use of the reflectarray topology for high power transmission includes reflection amplifiers and varactors on every element of the reflectarray. Reflection amplifiers are active devices that show a reflection coefficient greater than one at their input port. In this topology, a pilot signal would be transmitted towards the reflectarray, and each reflected wave from each element would have extra power from the reflection amplifier. The varactors can be electrically controlled to vary the phase of each reflecting element, thereby creating a method of controlling the phase distribution across the aperture and thus allowing for beam steering [11].

Which of these methods is the best for a power beaming scenario? A physical reflector

dish implies that the entirety of the transmitted power originates from a single feed at the focal point. Scaling the power level of a single transmitter to the megawatt regime and gigawatt regime for large scale power transfer presents unique challenges that are currently the subject of ongoing research (for example, [12]). In contrast, active phased array and active steerable reflectarray architectures have very good economies of scale. Power can be increased by simply increasing the number of transmitting elements in the array, which increases the focusing power by increasing physical area. Both can also be electronically steered without mechanical movement. Figure 1.2 shows the topology of an active steerable reflectarray compared to a phased array.

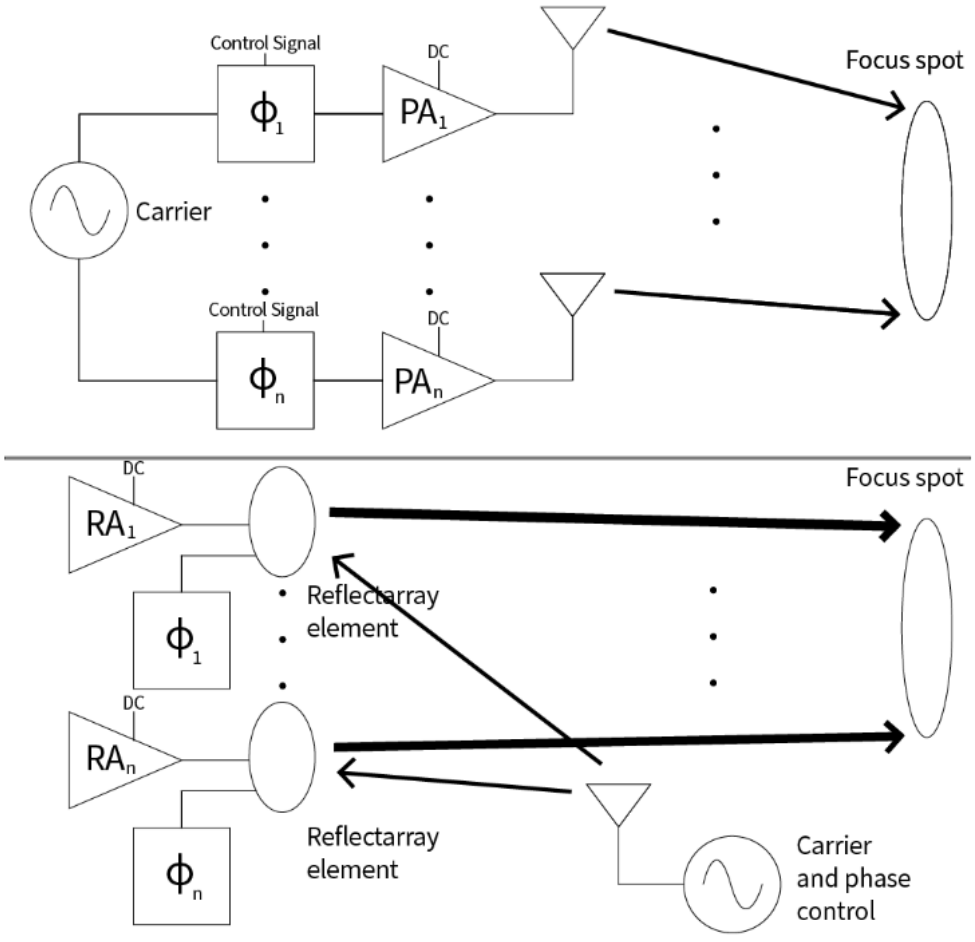

Figure 1.2: Simplified comparison between phased array and active reflectarray.

The primary advantage of an active steerable reflectarray is the removal of physical

connections to the RF carrier source. Instead, the carrier is transmitted to the surface of the reflectarray with a pilot signal. Additionally, in one potential implementation, the carrier could be accompanied by a phase control signal that controls the varactor phase. In this implementation, each unit cell of the reflectarray would only need to be physically connected to a DC power source to bias the varactor and power the reflection amplifier. This could have significant practical implications for systems such as Space Solar Power, where each unit cell of the transmit satellite could be entirely physically self contained, simplifying satellite construction and allowing for lower cost large transmit apertures due to the decreased cost of additional transmit elements.

Reflectarray elements are tuned initially by adjusting the physical geometry of each element. In [7] and [13], the side length and radius of square and circle patches respectively are tuned to generate the required reflection phase across the surface of the reflectarray. However, the phase of each element shows very fast variation with respect to physical geometry around the resonance point, which means that small changes in physical dimensions correspond to large changes in reflected phase. This directly leads to the result that plain square and circle patches require high manufacturing precision to maintain acceptable levels of phase error. This can potentially be addressed by modifying the unit cell design.

Several examples of retrodirective pilot beams transmitted from the receiver station to guide the pointing of a wireless power transfer system already exist in the literature [14][15][16]. Such a signal could be used as the reflectarray input signal, providing phase and a carrier signal to amplify. In this implementation, some of the complexity is loaded onto the receiver station, making the expensive transmitter more feasible to construct without high power feeds. In the archetypal example of Space Solar Power, this eliminates the need for a feed satellite to fly alongside the transmitting satellite.

This thesis aims to investigate several aspects of reflectarray design relevant to the implementation of a large-scale wireless power transfer system. The first is the effect of using a hexagonal unit cell rather than a square unit cell, as seen in many reflectarray studies.

This is investigated in Chapter 2. Next, Chapter 3 examines the use of several microstrip patch antenna geometries that could be applied to reflectarray unit cell design to increase degrees of freedom during design and decrease the phase slope of the tuning curve. Finally, Chapter 4 simulates the effect on hologram phase for two different ground station pilot signals incident on hypothetical active transmit reflectarrays.

CHAPTER 2
REFLECTARRAY GRID CHOICE

The central concept of a holographic reflectarray is to vary the amplitude and phase of the reflection coefficient across a surface such that the reflected wave from a given incoming wave will have a desired phase and amplitude distribution at the focal distance d. The term ”holographic” refers to the technique of generating Gabor holograms. In a Gabor hologram, recording the interference pattern of an incident wave and a desired image (i.e. desired amplitude and phase distribution) in the reflection coefficient of a surface produces the desired image when illuminated with said incident wave [17]. This has been extensively used in science and industry to create simple high gain antenna structures [18][19].

Since it is difficult to create a continuous variation of reflection coefficient across the surface, the holographic reflectarray instead discretizes the surface into array unit cell elements, where each element has a desired reflection coefficient. The array is also constrained to a plane, and the array is assumed to be large (i.e. containing a significant number of elements).

The combination of these decisions allows for simple simulation of the reflection coefficient of a single array element by idealizing the array as infinite in two dimensions and analyzing the reflection of a plane wave from a single unit cell[20]. By varying the geometry of the conducting element in the unit cell, some physical dimension can be plotted against the reflection coefficient of the cell, thereby creating a curve that can be used to size each array element given the desired reflection coefficient response. This procedure is discussed more in Section 2.0.1.

In much of the reflectarray literature, a rectilinear grid is used for the geometric placement of unit cell elements [20][21][13]. However, a hexagonal unit cell can also be used, which exhibits a higher packing efficiency and lower inter-element spacing than a square

unit cell for equal-width cell sizes. This configuration has been investigated in the context of 5G reflectarrays in [22] and in the context of high power wireless power transfer at L-band in [23]. A higher packing efficiency leads to higher metallization of the reflecting surface, which brings the magnitude of the reflection coefficient for the surface closer to 1. In practice, the phase distribution is much more dominant of an effect in terms of beam formation, but reducing amplitude perturbations within the reflectarray may provide benefit at no additional cost.

In this chapter, the effect of hexagonal and square grids are investigated on the phase and amplitude performance of unit cells. Section 2.0.1 first describes the methodology by which reflectarray unit cell element phase responses will be derived for this paper. In Section 2.0.2 and Section 2.0.3 the two grids are simulated separately using the procedure from Section 2.0.1 along with the effect of different substrates. It is found that hexagonal unit cells have very similar phase responses but tend to have larger $|S_{11}|$ at resonance. Section 2.0.4 discusses these comparisons in further detail.

2.0.1 Floquet Port Analysis

The idealization discussed at the beginning of this chapter can be implemented using Floquet ports and primary/secondary paired boundaries in Ansys HFSS. The Floquet port is used to simulate the incident wave and the primary/secondary paired boundaries are used to inform HFSS of the lattice directions. The general procedure derived from [7],[24],[25], and [26] for the simulation of a single unit cell is as follows:

1. Use the 3D modeling tools to create a single symmetrical unit cell of the reflectarray, consisting of a ground plane, substrate, array element, and air space above the array element.

2. Assign a Floquet port to the top of the air space. Specify the lattice directions according to the tessellation symmetry of the unit cell. De-embed the Floquet port to

reference the phase at the top face of the array element. An off-axis incident radiation angle of θ = 25 degrees was used in this project. ϕ = 0 is sufficient for the symmetrical element used in this project.

3. Assign primary/secondary boundary pairs to opposing faces of the air space, ensuring that the vectors for each boundary lie within the air space and that primary/secondary vector pairs are pointed in the same direction.

4. Add frequency sweep and/or parametric sweep of array geometry as needed and analyze.

2.0.2 Rectangular Grid

Following work in [7] and [13], a rectangular unit cell with a circular patch reflecting element is simulated using Ansys HFSS. This process can be seen in Figure 2.1. First, the unit cell is modeled as a slab of substrate with a thin slab of copper ground plane and a thin cylinder of copper as the patch element, as shown in Figure 2.1a. Next, the Floquet port is assigned to the top of the air box and de-embedded such that the calculated reflection phase is at the top surface of the patch element. A scan angle of θ = 25 degrees is included to simulate off-axis incident radiation. The lattice directions are chosen in the positive X and Y directions, although due to the symmetry of the unit cell, choosing negative X or Y directions should not influence the result. This is shown in Figure 2.1b. Figure 2.1c shows the assignment of one of the two Primary/Secondary boundary pairs required for the infinite lattice simulation. Notice that each set of u,v vectors for the boundaries are matched in direction and lie entirely on the edge of the air box. Finally, to simulate the effect of changing the patch size, a parametric sweep on the patch radius is added at 5.8 GHz in Figure 2.1d.

Table 2.1 shows the 4 parametric sweeps done to confirm the results of [7]. The air box height used was 30mm and the thickness of the copper layers was set to 1.4 mil (1

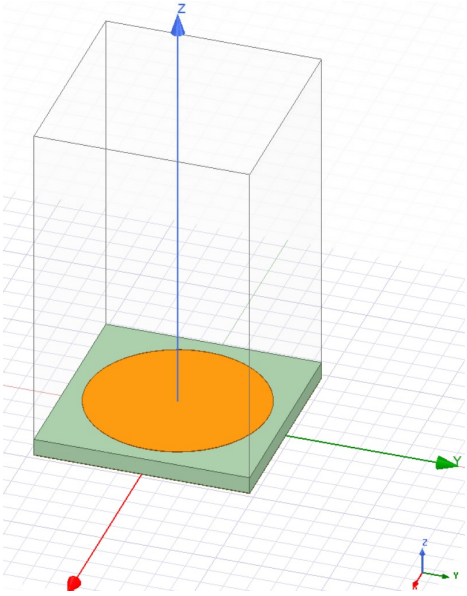

(a) 3D geometry

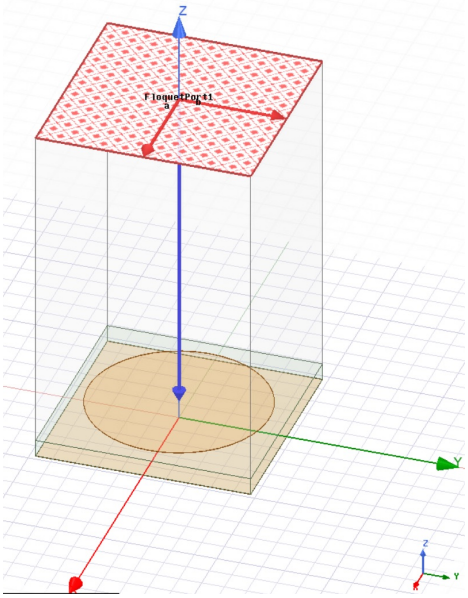

(b) Floquet port with lattice directions specified

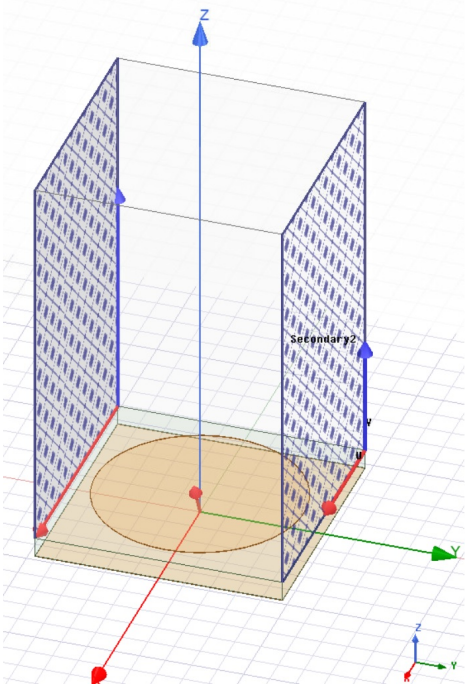

(c) First set of Primary/Secondary boundaries specified

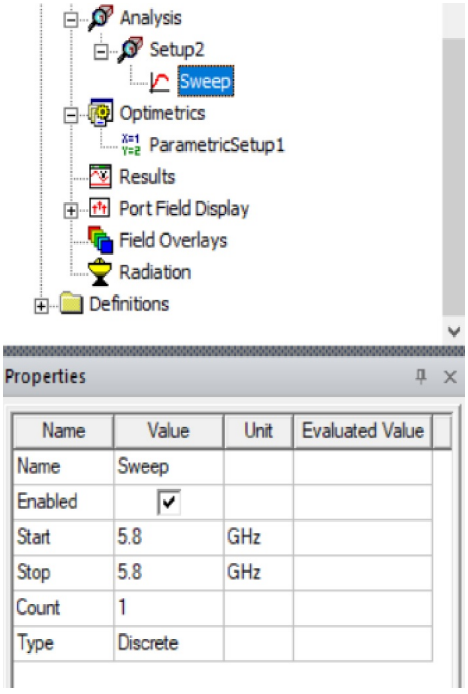

(d) Sweep setup

Figure 2.1: Floquet simulation setup for square unit cell in ANSYS HFSS.

ounce copper) for all simulation runs. It was found in [7] that the effect of changing from 0.5 ounce copper to 1 ounce copper for the ground plane and patch element for the same substrate and substrate thickness negligibly affected the phase response, so this parameter is not investigated further.

Table 2.1: Simulation variables for sub-wavelength circular patches on a rectilinear grid.

Substrate	Relative Permittivity	Substrate Thickness	Patch Radius	Cell Size
FR-4	4.4	60 mil (1.524mm)	4mm to 8mm	19mm×19mm
FR-4	4.4	118.11 mil (3mm)	4mm to 8mm	19mm×19mm
RO4003C	3.55	60 mil (1.524mm)	4mm to 8mm	19mm×19mm
RO4003C	3.55	20 mil (0.508mm)	4mm to 8mm	19mm×19mm

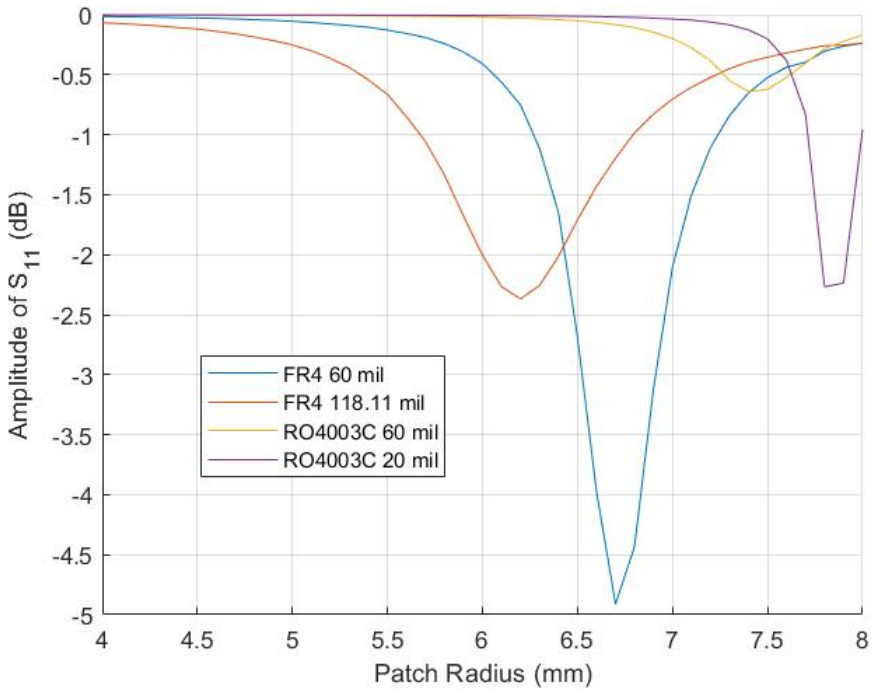

Figure 2.2: Magnitude of the reflection coefficient S_{11} versus patch radius for a square grid and circular patch element for varying substrates and substrate thicknesses.

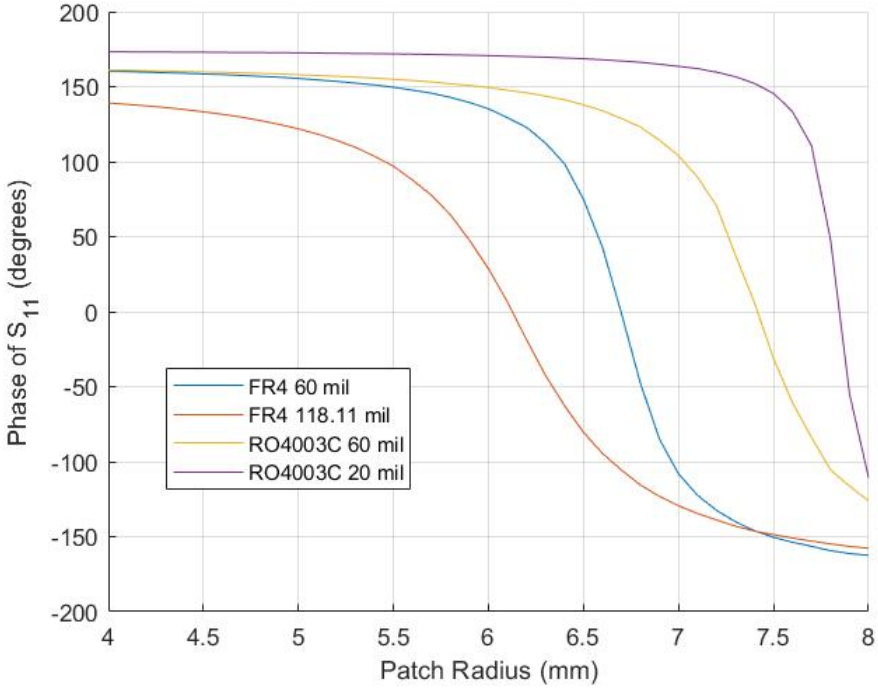

Figure 2.3: Phase of the reflection coefficient S_{11} versus patch radius for a square grid and circular patch element for varying substrates and substrate thicknesses.

Figure 2.2 shows that changing the substrate from lossy FR-4 with a higher dielectric constant to low-loss Rogers RO4003C with a lower dielectric constant shifts the resonance of the patch element to a larger patch radius, as well as increases reflection efficiency (close to 0 dB S_{11}). For both substrates, the depth of the resonance valley follows the thickness of the substrate inversely, such that thinner substrates lead to deeper (less reflective) resonant valleys. For a reflector system, a reflection coefficient close to 1 is desired, so thicker substrates appear to perform better in this regard.

The phase curves of each unit cell element with a rectilinear grid and varying substrates are shown in Figure 2.3. As expected from the above magnitude graph, the resonance point (phase = 0) of the unit cell element is shifted towards a larger patch radius when an identically thick substrate with lower permittivity and loss is used. Of particular note in Figure 2.3 is the phase curve behavior with respect to substrate thickness. When the 20 mil RO4003C is used, the phase curve is nearly vertical, with nearly the entire phase

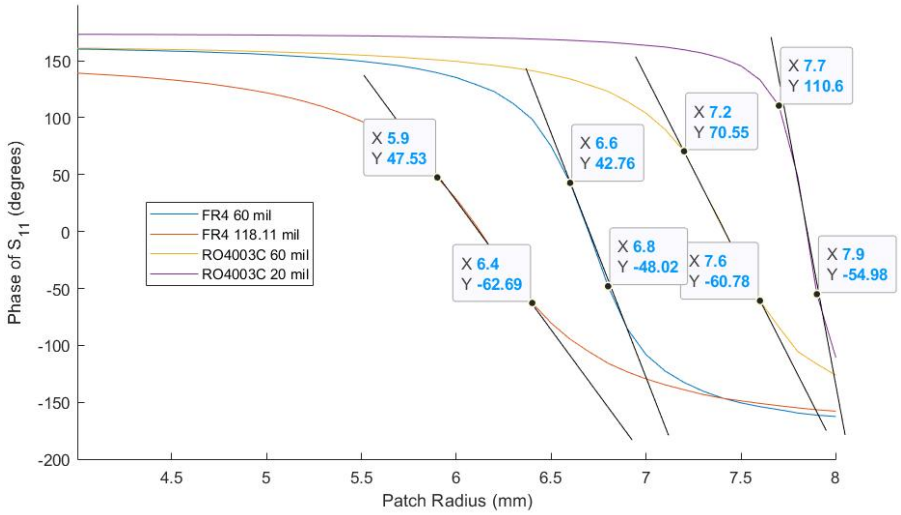

Figure 2.4: Phase curve with marked points in the approximately linear region for slope determination.

tuning range in between 7.7 and 8 millimeters. In comparison, the 3mm thick (118.11 mil) FR-4 has a much less steep phase curve, spreading out the phase variation over 5.5 to 7 millimeters. These results are in good agreement with the results from [7].

The slope of the phase curve is important to consider when implementing a real reflectarray for a wireless power transfer system. This is due to the effect of manufacturing tolerance on the actual phase behavior of a given unit cell element. If the phase curve is steep, like in the 20mm RO4003C case, then even less than a 0.1mm (4 mil) variation near resonance can cause a phase change of over 50 degrees, and it becomes very difficult to accurately form the reflectarray. Figure 2.4 adds markers to the phase curves to calculate the highest rate of phase change for each curve. Table 2.2 summarizes the effect of different substrates on the rectangular grid elements.

2.0.3 Hexagonal Grid

The investigation into the effect of a hexagonal unit cell for the wireless power transfer reflectarray begins with a similar simulation setup as in Section 2.0.1. Figure 2.6 shows the Floquet port analysis procedure in Ansys HFSS for the hexagonal unit cell. The Regular

Table 2.2: Summary of rectilinear grid reflection responses.

Substrate	Relative Permittivity	Substrate Thickness	Phase Range	Maximum Phase Slope	Reflection Coefficient Minimum
FR-4	4.4	60 mil (1.524mm)	323 degrees	454 deg/mm	-4.9 dB
FR-4	4.4	118.11 mil (3mm)	296 degrees	221 deg/mm	-2.37 dB
RO4003C	3.55	60 mil (1.524mm)	325 degrees	328 deg/mm	-0.62 dB
RO4003C	3.55	20 mil (0.508mm)	346 degrees	828 deg/mm	-2.3 dB

Polyhedron tool is used to create the substrate, ground plane, and air box, and the circular patch element is again made using the Cylinder tool. To maintain the same inter-element spacing as the square unit cell, the geometry is laid out as seen in Figure 2.5.

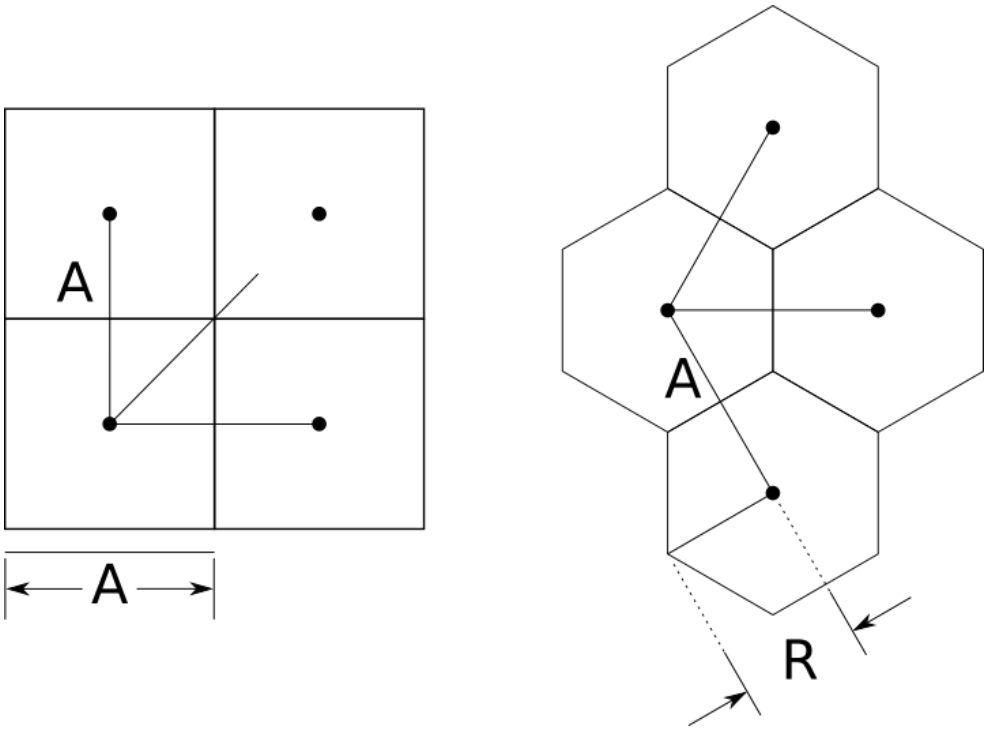

Figure 2.5: Geometry of the two unit cells investigated. Image created using Inkscape.

The Polyhedron tool defines the hexagonal substrate using its outer radius R. The inter-element spacing A between two of the hexagonal unit cells is $\sqrt{3}\times$R. If A has been defined

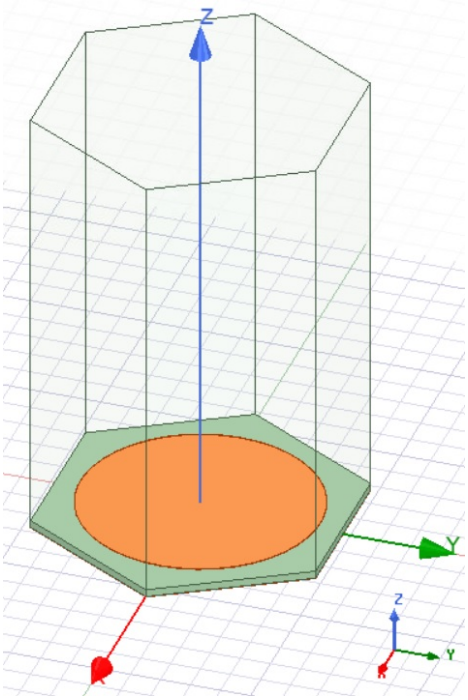

(a) 3D model

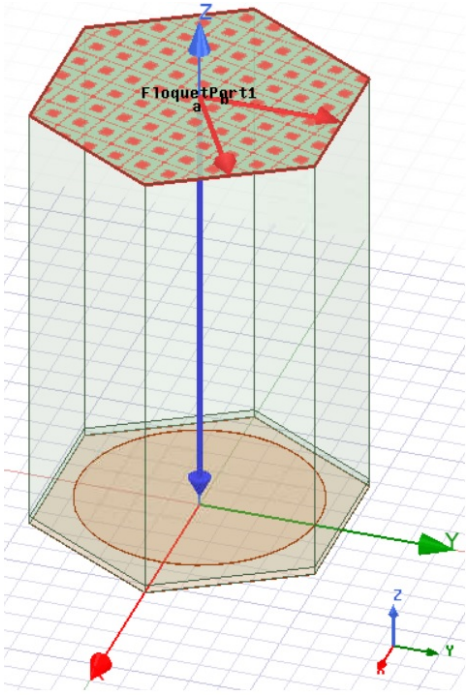

(b) Floquet port with lattice directions specified

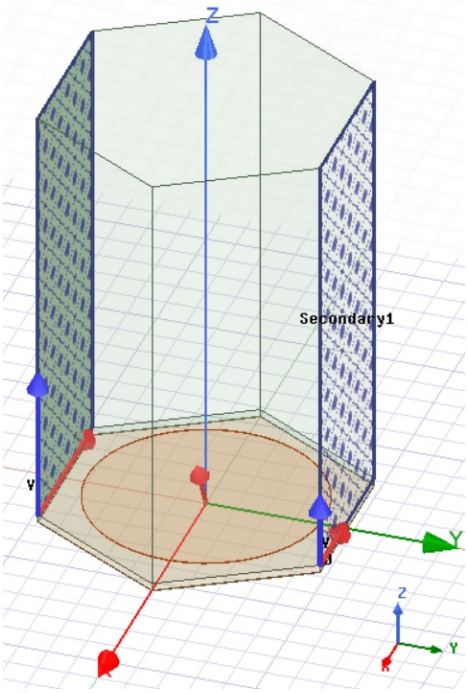

(c) First set of Primary/Secondary boundaries specified out of 3 total pairs

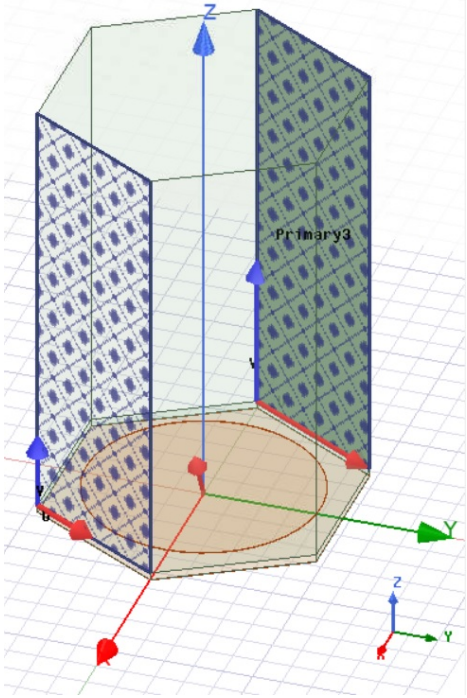

(d) Second set of Primary/Secondary boundaries specified out of 3 total pairs

Figure 2.6: Floquet simulation setup for hexagonal unit cell in ANSYS HFSS.

to be 19mm as in the square unit cell case, then R can be easily solved as $\frac{A}{\sqrt{3}}$ = R = $\frac{19mm}{\sqrt{3}} \simeq$ 10.97mm. Note that this inter-element spacing is constant for all elements in the hexagonal unit cell case, but is not constant for the diagonal unit cells in the square unit cell case. This geometric fact along with the higher packing efficiency may account for differences in the phase tuning curves between the two unit cell shapes.

After the cell radius is determined, a Floquet port with θ = 25 degrees and de-embedded to the top of the patch element is placed at the top of the air box in Figure 2.6b. The lattice directions are 60 degrees from each other instead of 90 as in the square case. Finally, three pairs of Primary/Secondary radiation boundaries are set around the 6 side faces of the air box, shown in Figure 2.6c and Figure 2.6d.

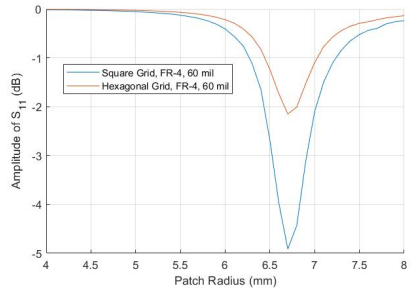

(a) FR-4, 60 mil

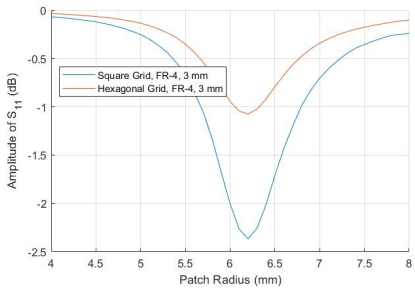

(b) FR-4, 3 mm (118.11 mil)

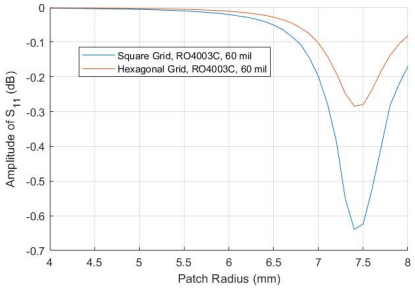

(c) RO4003C, 60 mil

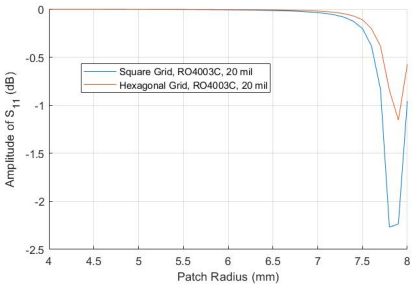

(d) RO4003C, 20 mil

Figure 2.7: Magnitude of the reflection coefficient S_{11} versus patch radius for a hexagonal grid and circular patch element for varying substrates and substrate thicknesses, compared to square grid results.

Figure 2.7 gives the result that the depth of the magnitude valleys at resonance for all substrates is raised by 1 to 2 dB for the hexagonal unit cell, meaning more power is reflected rather than absorbed at resonance than the square unit cell. This intuitively follows

as a result of the higher packing efficiency argument, with less energy "falling between" the individual patch elements and dissipating in the substrate. Section 2.0.4 explores this concept further.

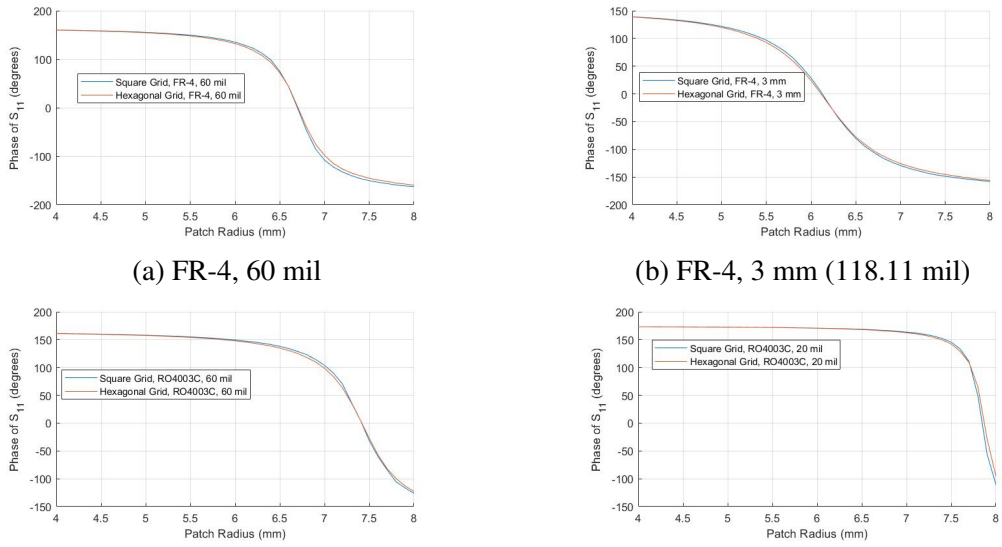

(a) FR-4, 60 mil

(b) FR-4, 3 mm (118.11 mil)

(c) RO4003C, 60 mil

(d) RO4003C, 20 mil

Figure 2.8: Phase of the reflection coefficient S_{11} versus patch radius for a hexagonal grid and circular patch element for varying substrates and substrate thicknesses.

In contrast, the phase tuning curve for the hexagonal unit cell element was virtually indistinguishable from the rectilinear grid. Figure 2.8 shows that for each substrate, the phase curve with patch size did not change. This can also be inferred from Figure 2.7, where the width of each resonant valley for the two unit cell geometries also remained constant.

Since the phase range, maximum phase slope, and location of resonance all did not change for a constant inter-element spacing change in unit cell geometry, this substitution can be made freely for a wireless power transfer design. The only effect that the hexagonal unit cell provides is a positive one - increasing the magnitude of the reflection response near resonance.

2.0.4 Comparisons and Recommendations

A wireless power transfer system in the microwave regime by necessity must have aperture areas on the transmit and receive sides that allow for Fresnel focusing to obtain a high power transfer efficiency [3]. This means that the transmit and receive apertures must be physically and electrically large. A large physical structure will have a high material and manufacturing cost. However, these costs can potentially be lowered by choosing aspects of the reflectarray design carefully: i.e. trading performance for cost.

Gaussian Error Analysis

One significant tradeoff that is evident in this study is the relationship between substrate thickness, phase range, and maximum phase slope. As substrate thickness increases, the phase range of a unit cell element decreases, but the maximum phase slope also decreases. For example, for the 3mm thick FR-4 substrate unit cells, the phase range is slightly under 300 degrees, which can lead to phase error when creating the reflectarray hologram. Compared to the other substrate thicknesses, however, the maximum phase slope is $\frac{2}{3}$ to even $\frac{1}{4}$ as much.

The effect of lowering the maximum phase slope can be illustrated by a hypothetical example. Suppose that for a particularly large reflectarray, phase errors of ± 15 degrees are allowed per unit cell and the system can still work. This has good agreement with the results from [7], which showed that this level of phase error is acceptable. First, we assume that the patch radius has a standard normal distribution due to the statistical imperfection of a given manufacturing process. To get 95% confidence that the phase will lie between ± 15 degrees of the desired phase, the phase must have a standard deviation of 7.65 degrees. This can be calculated using the standard z-tables for the normal distribution; ± 1.96 standard deviations away from the mean gives a 95% confidence interval. Assuming the desired phase is 0, we can linearize the phase tuning curves using the maximum phase slope as the slope of a line passing through the resonance point. The relation between patch size and

phase is therefore:

$$\Phi(patchsize) = -patchsize \times MaximumPhaseSlope + ResonantPatchSize \quad (2.1)$$

The relationship between variances for a random variable Y that is a linear transformation of another random variable X ($Y = mX + B$) is:

$$Var(Y) = m^2 * Var(X) \quad (2.2)$$

Therefore,

$$Var(\Phi) = 7.65^2 = m^2 * Var(X) \quad (2.3)$$

$$\frac{7.65^2}{m^2} = Var(X) \quad (2.4)$$

$$\sqrt{\frac{7.65^2}{m^2}} = \sigma(X) \quad (2.5)$$

Table 2.3: Manufacturing tolerance comparison for different substrates.

Substrate	FR-4 60 mil	FR-4 3 mm	RO4003C 60 mil	RO4003C 20 mil
Maximum Phase Slope	454 deg/mm	221 deg/mm	328 deg/mm	828 deg/mm
Required Manufacturing Tolerance	±0.033mm (±1.3mil)	±0.069mm (±2.7mil)	±0.047mm (±1.85mil)	±0.018mm (±0.7mil)

Table 2.3 shows the results of this basic Gaussian error propagation analysis. The "Required Manufacturing Tolerance" row is calculated by using Equation (2.5) and multiplying by ±1.96 to obtain the 95% confidence interval. In many cases, the tolerance for a PCB manufacturer using standard PCB etching methods may be ±2 mils (±0.051 mm) [27], which would be insufficient to meet the ±15 degree phase tolerance requirement around resonance for all of the tested substrates except for the 3mm FR-4. Tolerances much smaller than this can be achieved: ±1 mil (±0.025 mm) tolerance is also available at many PCB

manufacturers, but this comes at a greater cost. For a large reflectarray, this increased manufacturing cost might be prohibitive. Therefore, it is recommended that a thicker substrate be used for large scale reflectarrays.

Basic Cost Analysis

Along with the increased tolerance requirement, the cost disparity between FR-4 and Rogers RO4003C is extremely high. A basic cost analysis is shown in Table 2.4[28][29]. This cost analysis only considers the cost of the raw material - no handling, further processing, or installation costs are considered. RO4003C (along with many specialty RF substrates) are extremely expensive compared to FR-4. This is due to some degree to the economies of scale that FR-4 enjoys compared to RF substrates, but tightly controlled fiberglass laminates are inherently more costly to produce than FR-4. This effect can be seen in the magnitude plots of all of the RO4003C substrate simulations. In some cases, the loss at resonance can be as low as 0.3 dB. However, higher reflection losses can be compensated to a degree by using the higher packing efficiency hexagonal unit cell, so an expensive RF substrate does not appear to be necessary from this analysis.

Table 2.4: Cost comparison of RO4003C and FR-4.

Substrate	Cost Per Square Meter	Cost Ratio
FR-4	$4.36	1
Rogers RO4003C	$278 to $751	60 to 172

Packing Efficiency Analysis

The most intuitive explanation for the difference in reflected magnitude between hexagonal and square unit cells for a constant inter-element spacing is that the packing efficiency of hexagonal unit cells is higher. Figure 2.9 shows the calculated packing efficiency for both square and hexagonal unit cells using normalized patch element radius on the X axis and

packing efficiency in percentage on the Y axis. The formula for packing efficiency P is:

$$P = \frac{PatchArea}{TotalCellArea} \tag{2.6}$$

$$P_{square} = (\frac{\pi}{3})(\frac{r}{R})^2 \tag{2.7}$$

$$P_{hex} = (\frac{2\pi}{3\sqrt{3}})(\frac{r}{R})^2 \tag{2.8}$$

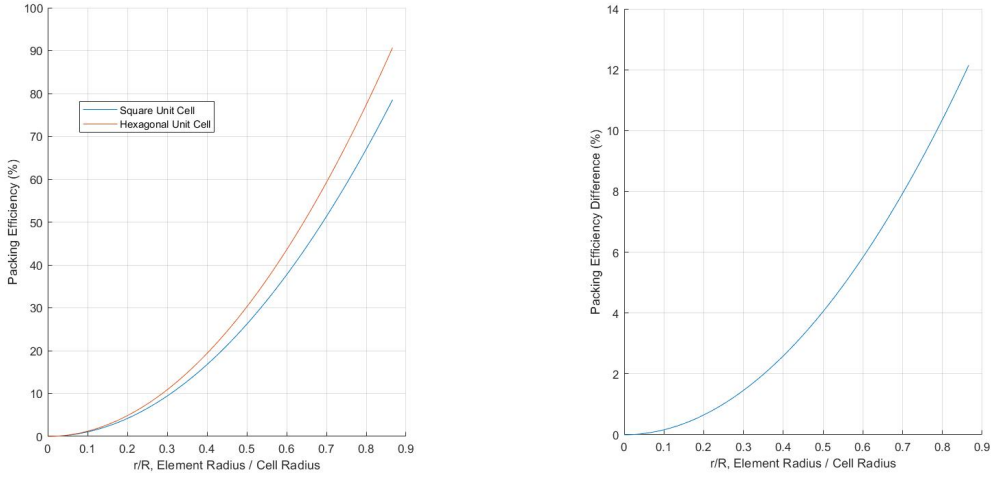

(a) Direct packing efficiency comparison.

(b) Difference in packing efficiency.

Figure 2.9: Comparison of packing efficiency between hexagonal and square unit cells for a constant inter-element spacing.

Using Equation (2.7) and Equation (2.8), Figure 2.9a is plotted up to $\frac{r}{R} = \frac{\sqrt{3}}{2}$. The phase ranges of these circular patch elements generally fall between radii of 6 to 8mm , meaning that the packing efficiency improves from between 4 to 8 percent using a hexagonal unit cell versus a square unit cell. The fact that there was no change in the phase tuning curve indicated that the increase in reflected power observed with the hexagonal reflectarray was not due to a resonance effect of the elements but most likely rather a simple increase due to higher metallization of the unit cell surface.

CHAPTER 3
REFLECTARRAY ELEMENT DESIGN

As discussed previously, cost is a primary driving constraint on the implementation of a wireless power transfer reflectarray due to the necessary aperture area requirement. Chapter 2 investigated circular patch elements with less than 0.5λ spacing, with a final hexagonal unit cell with a circular patch that could potentially be tolerant of up to $\pm$0.069mm ($\pm$2.7mil) of manufacturing error. While this is a fairly reasonable level of error for a standard PCB manufacturer, lowering the manufacturing requirements further to $\pm$0.127mm ($\pm$5mil) could allow extremely low cost etching or milling processes without any extra modifications to manufacture reflectarray cell elements. This extreme case might be needed in very large wireless power transfer scenarios, such as Space Solar Power, in which aperture areas on the ground and in orbit might exceed 4 kilometers in diameter. Therefore, modifying the simple circular patch element to investigate potential candidates for highly tolerant reflectarray elements is desirable.

In addition to lowering the manufacturing tolerance requirement, there is another consideration in attempting to synthesize alternative reflectarray elements. The Floquet unit cell analysis used throughout this work assumes that the unit cell under investigation is a single element in an infinite array of identical elements. This approximation is fairly good when there are no sharp physical discontinuities in the reflectarray surface. However, in areas where the phase changes rapidly or the edge of the reflectarray is close, then the Floquet infinite array approximation may not be as valid, leading to unpredictable behavior and degraded performance [18]. The more similar each reflectarray element is to one another, the more valid the Floquet infinite array approximation is. This provides the second of the two major criteria for developing a new wireless power transfer reflectarray element.

It should be noted that the frequency bandwidth of the unit cell is usually a primary

concern with reflectarray design. This is because many reflectarrays are used for communication purposes, such as deep space high gain antennas. These designs might require the use of multiple frequency bands using the same reflectarray. However, in a wireless power transfer scenario, it is expected that the frequency of operation will be essentially monochromatic. Even so, the bandwidth of a particular cell element would be expected to still be of significance when choosing a reflectarray element. A wider frequency bandwidth means that the phase of the reflection response varies over a larger frequency. Therefore, as the resonant frequency (controlled by some physical geometry) changes, a wider frequency bandwidth should logically also lead to a slower change in reflection phase as the physical geometry changes. It is demonstrated in this chapter that this relationship does not hold true in all cases.

Therefore, more techniques to lower the maximum phase slope of reflectarray unit cells are investigated. Section 3.0.1 begins the discussion with a review of the effect of inter-element spacing on reflectarray phase response. The remainder of the chapter presents results for Ansys HFSS simulations of the reflection responses for each of the modified circular patch elements.

3.0.1 Element Spacing

Inter-element spacing is a critical parameter for reflectarray design. A typical choice for the inter-element spacing of a reflectarray might be 0.5λ. At this spacing, each element can be self-resonant due to its electrically significant size. As the spacing and element size decrease, the individual elements stop exhibiting resonance on their own, but can start coupling with the adjacent elements, creating a coupled resonance effect that can also be used to adjust the phase distribution across the reflectarray. Reducing the inter element spacing in this manner creates ”sub-wavelength” reflectarrays. Sub-wavelength reflectarrays can be chosen to increase bandwidth and reduce element losses [18]. They allow for higher efficiency by reducing the amount of energy that “falls between” the elements and interacts

with the substrate and ground plane instead of the surface elements [30].

However, it has also been shown that reducing the inter-element spacing to sub-wavelength distances increases the slope of the relation between physical geometry of a patch element and the phase response of that element [18]. In a practical implementation, this means that a manufacturing variation of only 0.1mm in a physical feature in a unit cell element could lead to phase variations of 30 or more degrees. Previous work by [7], [13], and [23] in wireless power transfer reflectarrays use sub-wavelength reflecting elements. This work will explore the effect of 0.5λ spaced reflectarray elements as well.

The appearance of secondary grating lobes is a concern if the reflectarray is to be actively steered. [22] showed that for a 0.6λ spaced reflectarray at 8.23 GHz, the scan angle of a hexagonal reflectarray was improved to 60 degrees from 40 degrees with a square unit cell before grating lobes appeared in the radiation pattern.

Another factor to consider is the integration of active RF devices into the reflectarray architecture. A future reflectarray designed for a very long range wireless power transfer system would most likely require that each reflectarray element has an active oscillator phase locked to the incoming signal from the feed such that the power from every reflectarray element is spatially combined in air to provide power at the receiver. If the reflectarray were instead entirely passive, for a large array and high power levels, the feed(s) would have to handle large amounts of power, which decreases economies of scale - it is much easier to add power to a system by adding area to the transmitter/receiver than by designing a new very high power RF source. In addition to the power oscillator on each reflectarray element, phase control may be desirable so that multiple wireless power transfer customers can be serviced. These requirements lead to the result that each reflectarray unit cell must be physically large enough that active devices, along with their associated matching, feedback, and control networks, can be mounted to them. In addition, the unit cell electronics should be spaced enough to minimize the effect of mutual coupling, especially when considering low-cost transmission line networks to replace discrete components. The use of

sub-wavelength versus 0.5λ spacing should be considered carefully, so the following simulations in this chapter will consider both cases.

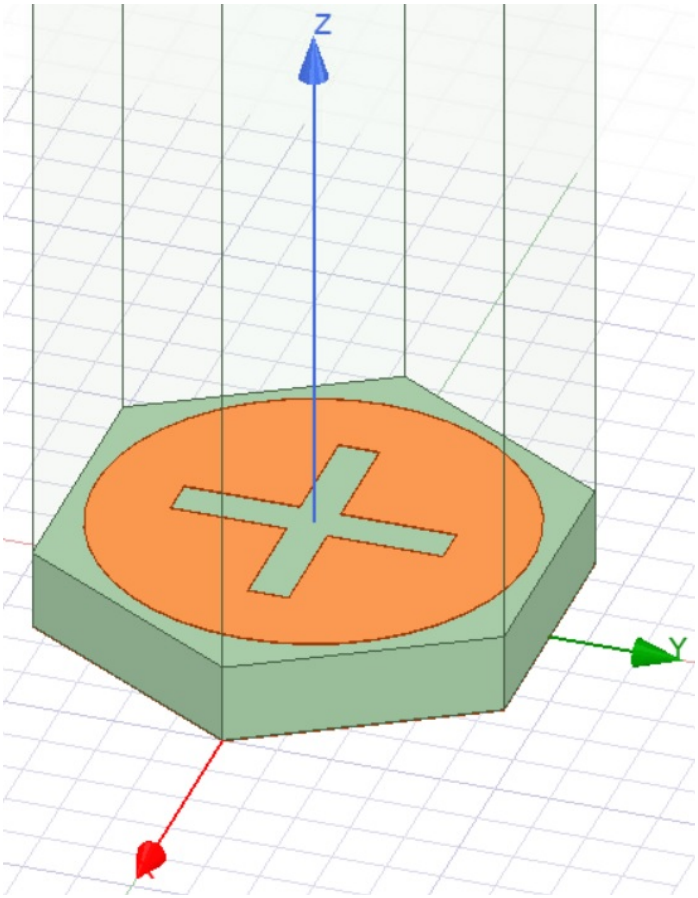

Figure 3.1: 3D model of circular patch with cross slot.

3.1 Circular Patch With Cross Slot

The first alternative reflectarray element examined is the circular patch with a cross slot in the center, shown in Figure 3.1. This configuration was examined in [31] for the case of a proximity-coupled microstrip patch antenna using an asymmetric cross to provide circularly polarized radiation. Of particular note in [31] is the observation that changing the slot length changes the resonant frequency of the overall patch. While the aim in that work was to reduce antenna size using this technique, shifting the resonant frequency by modifying the length of a geometric feature is equivalent to changing the phase of the

reflection from the structure at a single frequency. This is precisely the tuning behavior that is desirable for a reflectarray element.

Ansys HFSS simulation results for a circular patch loaded with a symmetric cross slot in the center are presented in this section. The primary aim is to provide reflectarray designers with another parameter to control the element phase to simultaneously minimize large geometric differences between adjacent elements and decrease the susceptibility of each element to manufacturing error. However, a more detailed economic analysis would be required to determine whether this improvement is worth the extra cost of fabricating the cross slot structure for each patch.

3.1.1 Sub-wavelength Spacing

The reflectarray element shown in Figure 3.1 is simulated using the parameters in Table 3.1. 3 millimeter thick FR-4 was chosen due to its superior phase performance found in Chapter 2, and the inter-element spacing was kept identical at 19mm to get an accurate comparison. The width of the slot was first varied between 0.5 and 1.5mm, and it was found that 1.5mm slot width reduced the phase range the least.

Table 3.1: Simulation parameters for sub-wavelength circular patch with cross slot.

Substrate	Inter-Element Spacing	Slot Width	Patch Radius	Slot Length
FR-4, 3mm thick, ϵ_r =4.4	19mm (0.367λ)	1.5mm	3 to 8 mm	3 to 10 mm

Since there are now two parameters that are varied to produce the full phase graph, the step size for each parameter is reduced to 0.5mm in order to increase simulation speed. Even so, the full simulation for each type of element requires up to 8 hours of processing time. Despite the low resolution, the overall phase behavior can easily be seen from Figure 3.2.

Figure 3.2 shows the effect of two characteristic "S-curves" simultaneously influencing the phase of the reflecting element to create a phase surface. It is apparent that the phase

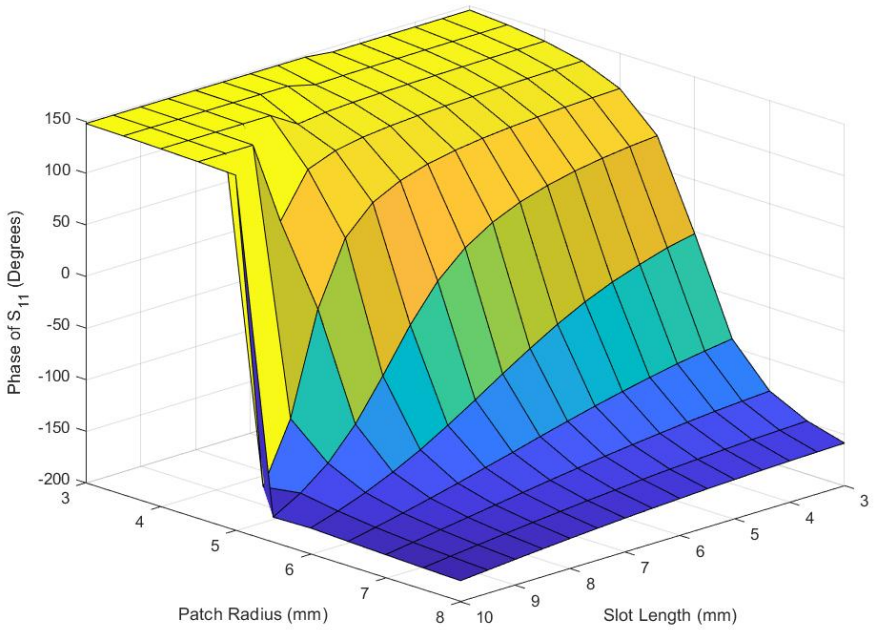

Figure 3.2: Phase surface for circular patch with cross slot with 0.367λ inter-element spacing.

curve with respect to slot length varies slowly at the expense of phase range. As an example, at a patch radius of 5.5mm, the maximum phase slope with respect to slot length is only 77 degrees/mm, which would make it easier to tune the patch using the slot length instead of the patch radius. In exchange for this slow variation in phase, the phase range at 5.5mm patch radius is only 256 degrees, far below the phase range of over 300 degrees that was achieved by [7] and [13]. However, if further phase range is required, it is evident that varying the patch radius at the same time can still achieve a large phase range of up to 328 degrees.

For example, consider the case if a phase shift of 0 degrees is required at one element, but the next element requires a 150 degree phase shift. Instead of having adjacent elements with over 3mm in radius difference, the patch radius can be changed by only around 1mm and then the slot length can be varied at the same time to achieve the 150 degree phase shift.

Figure 3.3 shows the magnitude surface created by variation in slot length and patch radius. There is a resonant "trough" present around the 5-7mm patch radius region, corresponding to the area of greatest phase variation around 0 degrees. The deepest resonance dip is -4 dB. Patch elements in this deep resonance region could exhibit too much loss and negatively impact the performance of the overall reflectarray. However, since there are two degrees of freedom available to achieve phase variation, this deep resonance peak can be avoided during hologram synthesis.

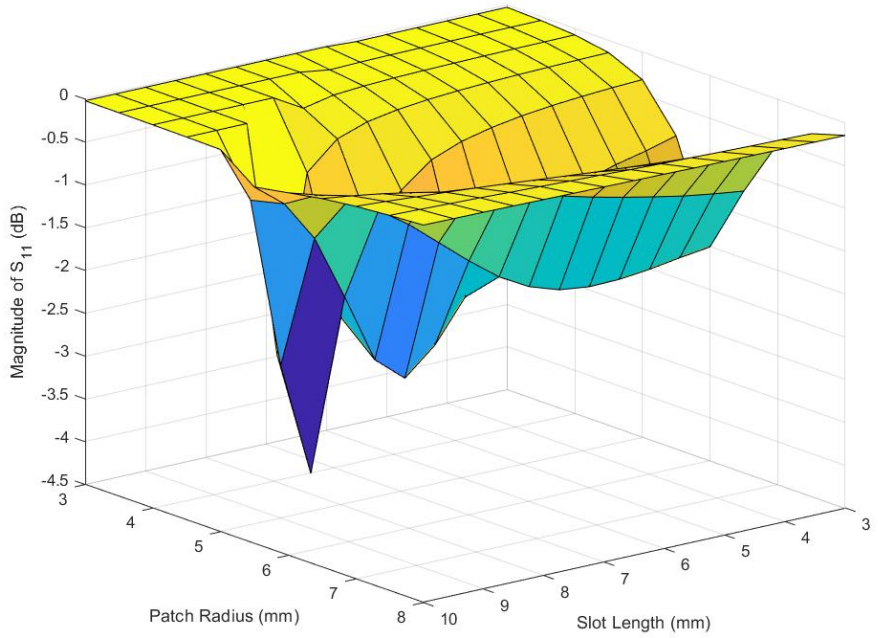

Figure 3.3: Magnitude surface for circular patch with cross slot with 0.367λ inter-element spacing.

It should be noted that there exist cases on the phase surface where the slot length is longer than the total patch diameter. For example, for a patch radius of 3mm, slot lengths of 6 to 10mm will result in slots that run through the entire diameter of the patch, forming four equal quarter-circles instead of a circular patch with a cross slot. Interestingly, the reflection behavior in the HFSS simulation does not appear to be affected by this. Physical prototyping and measurement of this could be of interest, but it is most likely that real-

world reflection behavior would drastically change once the patch is no longer a continuous conducting piece.

3.1.2 0.5λ Spacing

It is expected that increasing the inter-element spacing to 0.5λ will shift the phase tuning curve and decrease the maximum phase slope observed in agreement with [18]. The simulation parameters are updated according to Table 3.2. Preliminary coarse simulations were conducted to find bounds of interest for slot lengths and patch radii.

Table 3.2: Simulation parameters for 0.5λ spaced circular patch with cross slot.

Substrate	Inter-Element Spacing	Slot Width	Patch Radius	Slot Length
FR-4, 3mm thick, ϵ_r =4.4	25.9mm (0.5λ)	1.5mm	3 to 8 mm	3 to 9 mm

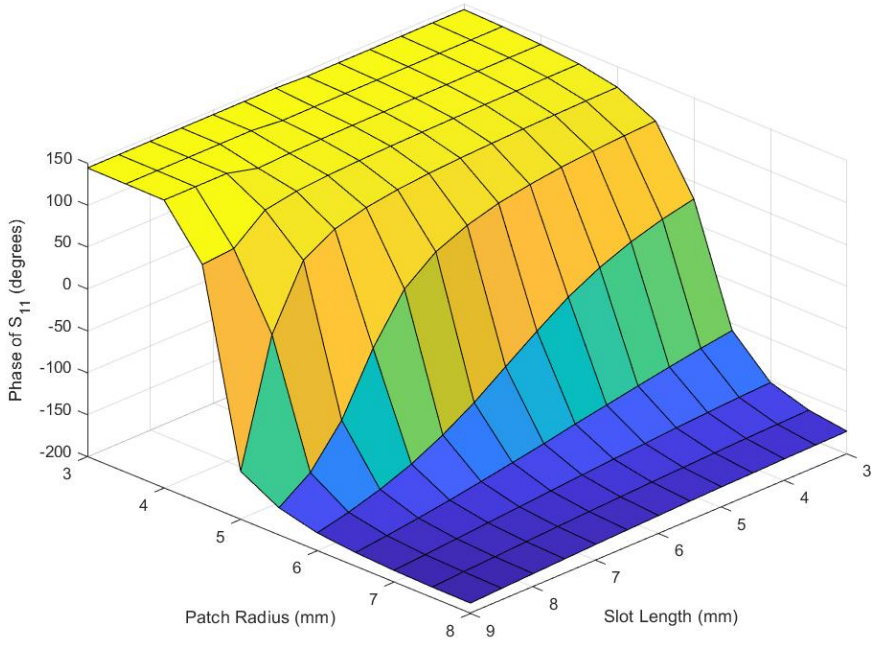

Figure 3.4: Phase surface for circular patch with cross slot with 0.5λ inter-element spacing.

Despite predictions to the contrary, the 0.5λ spaced reflectarray unit cell did not exhibit

notable differences in reflection behavior from the 0.367λ case. Figure 3.4 shows that the overall structure of the phase surface is identical to that of the 0.367λ case, and the phase slopes are very similar. The shift was still large enough that the phase surfaces are not interchangeable for the purposes of hologram synthesis, but the reflection behavior is similar enough that the 0.5λ spaced variant offers no clear benefit with regard to phase response for reflectarray design.

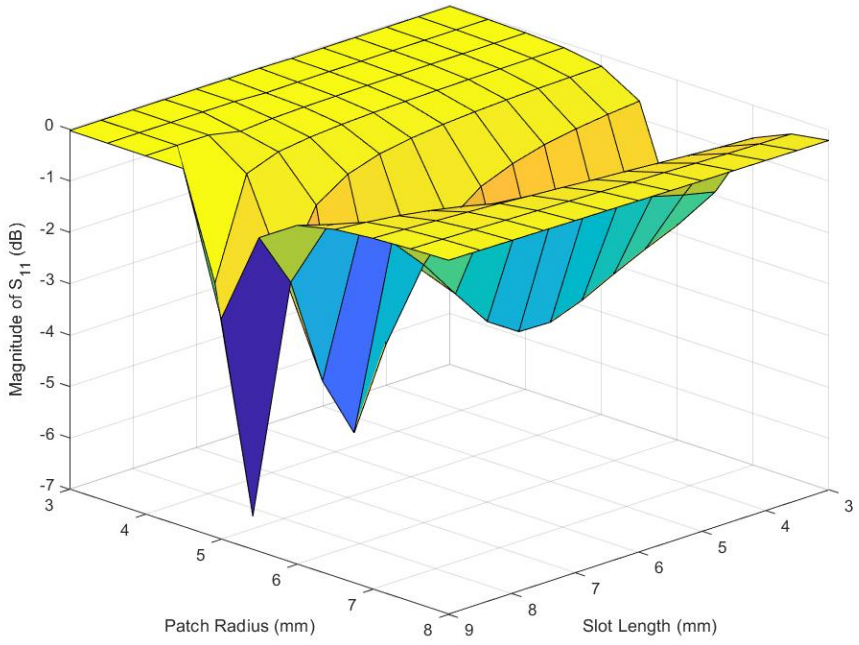

Figure 3.5: Magnitude surface for circular patch with cross slot with 0.5λ inter-element spacing.

In fact, the magnitude of the reflection coefficient drops up to -6.7 dB for the 0.5λ spaced unit cell. This is almost -3 dB lower than the deepest dip in the 0.367λ spaced unit cell. In general, the magnitude of the reflection coefficient of the larger spacing unit cell was lower at resonance. This can most likely be attributed to the lower proportion of reflecting surface area as a direct result of the larger inter-element spacing.

While there is no discernible benefit in the phase response of the 0.5λ spaced unit cell over the 0.367λ spaced unit cell, the larger unit cell area could still be useful with regard to

attaching electronics to each reflectarray element. A future wireless power transfer system would have to evaluate the tradeoff between reflection coefficient magnitude and usable unit cell surface area.

3.2 Circular Patch With Ring Slot

While the cross slot load introduced in the previous section was able to achieve a large phase response with multiple tunable parameters, there could be manufacturing issues with the sharp corners of the cross slot, especially with very low cost PCB etching techniques. Another reflectarray element is investigated in this section that could be easier to manufacture and maintains identical patch size to further reduce errors introduced by the Floquet infinite array assumption.

This unit cell element is shown in Figure 3.6. The structure consists of a variable size patch with a concentric annular ring with a constant outer diameter. The spacing between the patch and the ring is kept constant, and the reflection phase is tuned by varying the center patch radius.

Similar designs can be found in the literature, such as in [32],[33] and [34]. These works focus on increasing the bandwidth of an annular ring microstrip antenna using a parasitically coupled center patch. The proposed mechanism in [35] is that the resonant frequencies of the two conductors are close to each other and the overall bandwidth is determined by the superposition of the two responses. However, these designs are for actively fed antennas, and resemble the present investigated structure only when considering the top conductor layout. For example, [32] also includes a cavity resonator behind the antenna, and [33] stacks another circular patch underneath for dual-band operation.

3.2.1 Sub-wavelength Spacing

Unfortunately, due to the large physical differences between the structures in the literature and the present investigated reflectarray element, the increase in bandwidth for the antennas

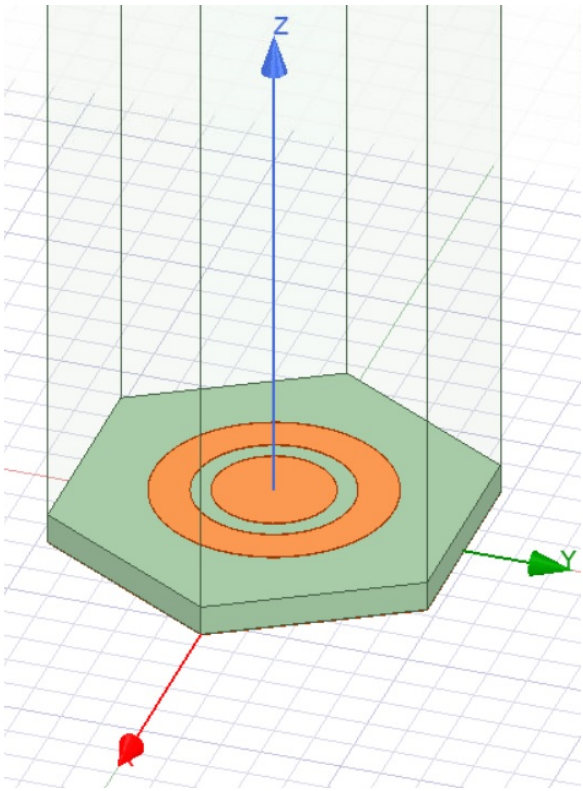

Figure 3.6: 3D model of circular patch with ring slot.

did not manifest in a larger physical tuning range for the reflectarray element. Simulations over a large variety of physical parameters were performed, and it was found that only the parameters detailed in Table 3.3 allowed for phase tuning.

Table 3.3: Simulation parameters for 0.367λ spaced circular patch with ring slot.

Substrate	Inter-Element Spacing	Slot Width	Patch Radius	Ring Radius
FR-4, 60 mil (1.524mm) thick, ϵ_r =4.4	19mm (0.367λ)	1mm	6mm	1 to 5 mm

The results of the above simulation are shown in Figure 3.7 and Figure 3.8. The essential problem is that this particular structure is very sensitive to the radius of the outer patch and the substrate thickness. This indicates that despite the fact that the corresponding antennas in literature enjoyed larger bandwidths, the present structure differed enough that insights from the literature did not translate well.

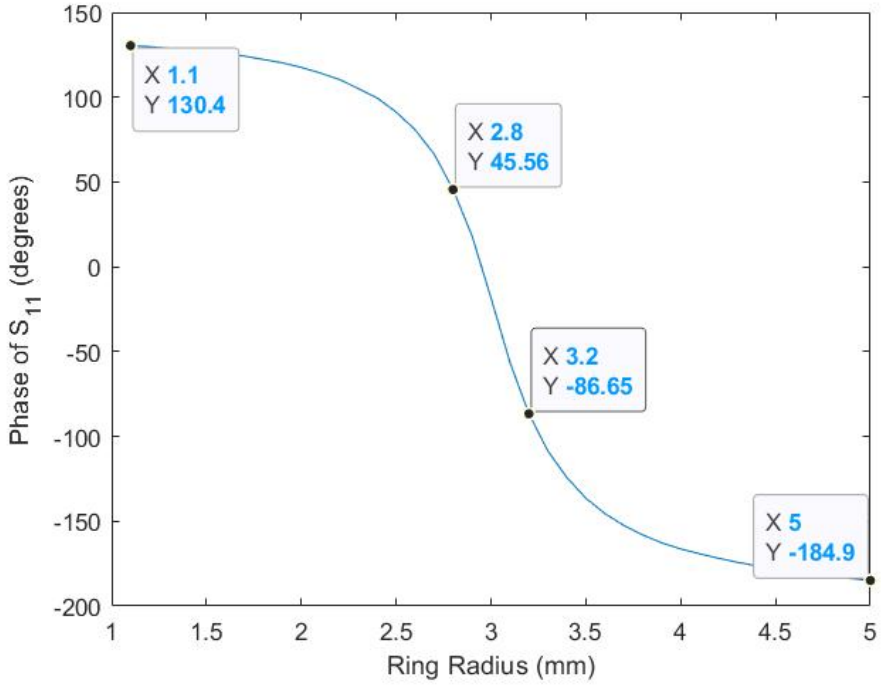

Figure 3.7: Phase of reflection coefficient for a circular patch with ring slot with 0.367λ inter-element spacing.

Figure 3.7 shows that while the phase range of the ring slot is sufficient at 315 degrees, the maximum phase slope is 330 degrees/mm, which is even higher than that achieved by the plain circular patch on 3mm FR-4 substrate from Chapter 2. This is also at the expense of a more complicated physical structure that would cost more to manufacture. Finally, the minimum value of the magnitude of the reflection coefficient in Figure 3.8 at the resonance point is -6.8 dB, which is almost the same level of loss as the lowest point of the circular patch with cross slot at 0.5λ spacing, but without the added advantage of more physical space.

3.2.2 0.5λ Spacing

The lowering of phase slope effect described in [textbook] was also not observed when the reflectarray inter-element spacing increased to 0.5λ. The parameters from Table 3.3 were nearly unchanged, as seen in Table 3.4. It is possible that by increasing the inter-element

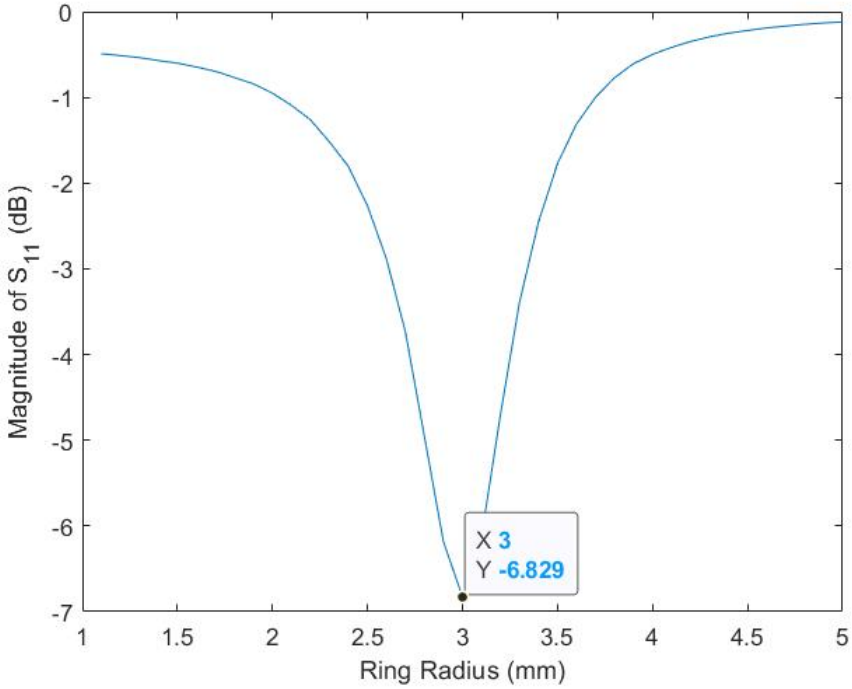

Figure 3.8: Magnitude of reflection coefficient for a circular patch with ring slot with 0.367λ inter-element spacing.

spacing further, the phase slope would decrease, but this would most likely be accompanied by even lower reflection.

Table 3.4: Simulation parameters for 0.5λ spaced circular patch with ring slot.

Substrate	Inter-Element Spacing	Slot Width	Patch Radius	Ring Radius
FR-4, 60 mil (1.524mm) thick, ϵ_r =4.4	25.9mm (0.5λ)	1mm	6mm	1 to 5 mm

As seen in Figure 3.9, the resonance point did not change from 3mm ring radius between the two inter-element spacings. The phase range also did not change drastically; it increased to 330 degrees from 315 degrees. However, the maximum phase slope also increased to 720 degrees/mm, which is extremely high and would require very precise manufacturing to maintain an acceptable amount of phase error.

The magnitude of the reflection response dips to -13 dB at resonance, which is far lower

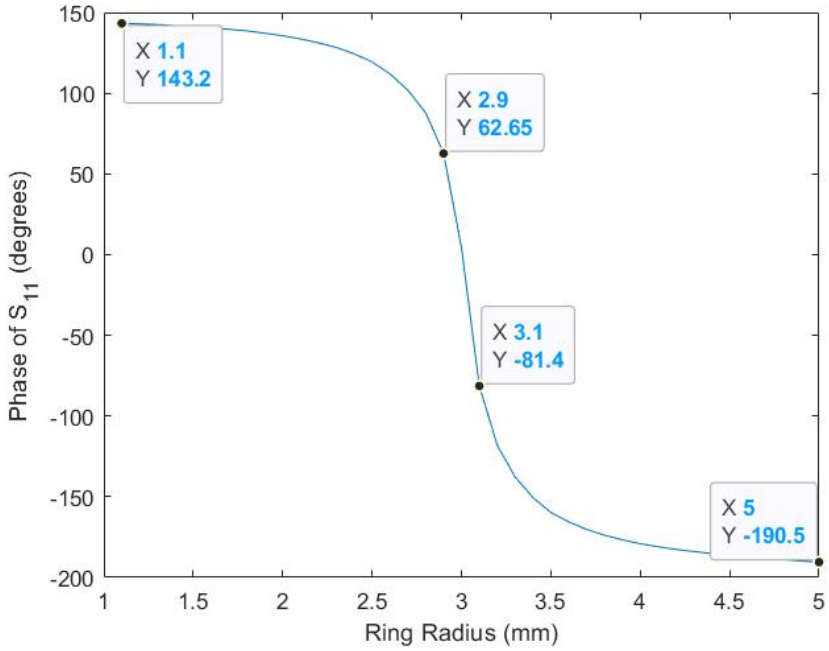

Figure 3.9: Phase of reflection coefficient for a circular patch with ring slot with 0.5λ inter-element spacing.

than the elements investigated thus far. Consistent with findings from Section 3.1, the larger spacing appears to lower the magnitude of the reflection from the unit cell. Overall, there is little advantage to using the 0.5λ spaced version of this unit cell element, especially over the circular patch with a cross slot. That structure shows both superior phase and magnitude response for the sub-wavelength and 0.5λ versions, and also allows for two degrees of freedom in choosing the unit cell phase.

3.3 Circular Patch With Exterior Slots

The third reflectarray element considered is the circular patch loaded with exterior slots, shown in Figure 3.11. By adding variable length radial slots originating from the exterior diameter of the circular patch, the phase can be tuned with 2 degrees of freedom, similar to the circular patch with cross slot examined in Section 3.1. [36] discusses a stacked microstrip antenna with a circular patch with exterior slots coupled to a turnstile antenna, in which the exterior slot lengths are modified to adjust the patch impedance. This tuning

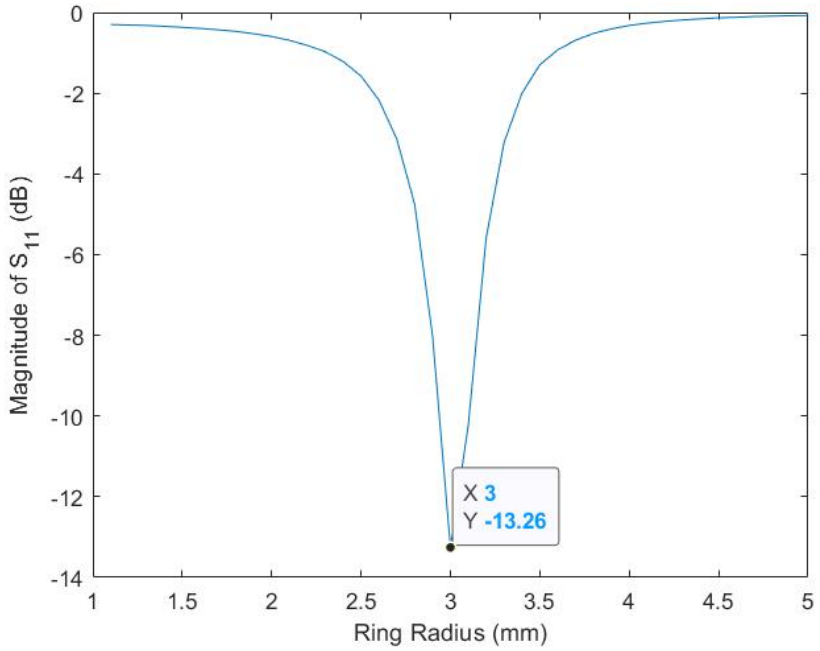

Figure 3.10: Magnitude of reflection coefficient for a circular patch with ring slot with 0.5λ inter-element spacing.

behavior is desirable for a reflectarray antenna as well. In addition, [37] provides further evidence of changing resonant frequency as the lengths of exterior slots change.

The purpose of this section is to investigate the performance of the exterior slot structure in comparison to the previous structures. Both this exterior slot element and the cross slot element have two degrees of freedom in tuning the phase of the reflection coefficient, so other advantages should be investigated in order to differentiate between the two.

3.3.1 Sub-wavelength Spacing

First, a rough parameter analysis was performed to find suitable ranges for the patch radius and slot lengths. This resulted in the parameters in Table 3.5. The same inter-element spacing as the original circular patch was used, and the phase and magnitude responses are displayed in Figure 3.12 and Figure 3.13.

Similarly to Section 3.1, the simulation used steps of 0.5mm to obtain the general shape of the phase surface. A finer step size of less than 0.1mm is desirable for a final hologram

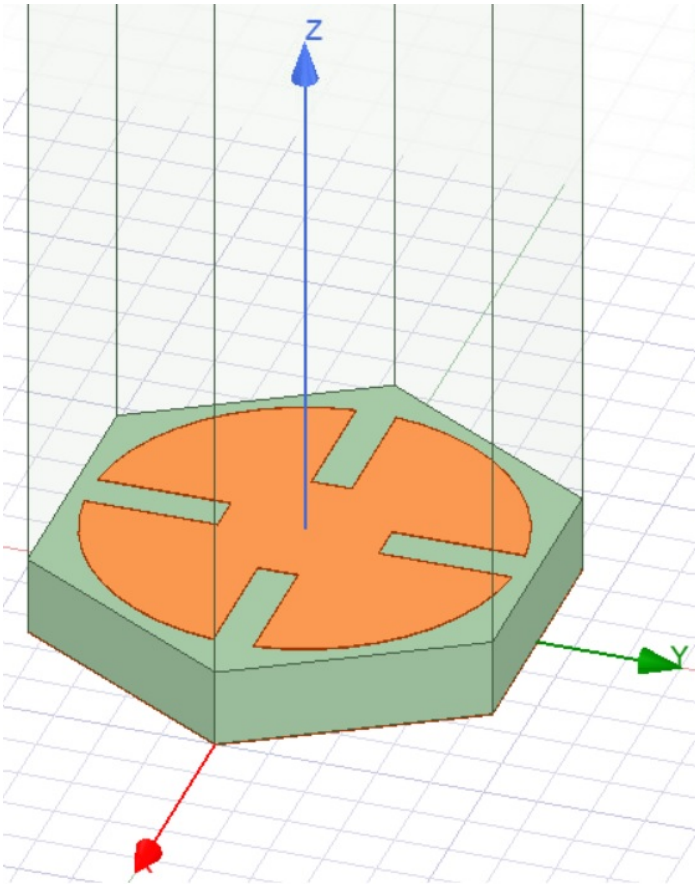

Figure 3.11: 3D model of circular patch with exterior slots.

design. However, large amounts of processing power would need to be allocated to this, as the current rough mesh surfaces shown were generated over 6+ hours.

Overall, the phase surface for the exterior slotted element shows remarkable similarity to that of the cross slot element. The phase range is very similar to the cross slot element at 329 degrees (compared to 328 degrees). In addition, it can be seen that at small patch radii and large slot lengths, the slots merge and the patch is no longer continuous. This can be seen in the irregularity near the top left corner of the graph.

However, the magnitude surface of the reflection response shows a slight improvement over that of the sub-wavelength cross slot patch of about 1 dB. While this small difference is largely inconsequential for the purposes of a reflectarray antenna, it is still a differentiating factor for elements that are so similar.

Table 3.5: Simulation parameters for 0.367λ spaced circular patch with exterior slots.

Substrate	Inter-Element Spacing	Slot Width	Patch Radius	Slot Length
FR-4, 3mm thick, ϵ_r =4.4	19mm (0.367λ)	1.5mm	4 to 8mm	1 to 5mm

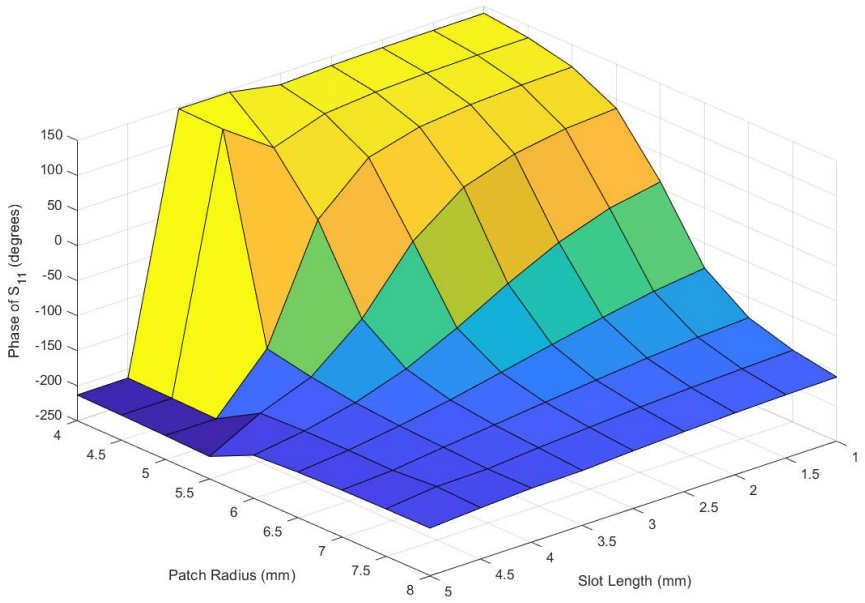

Figure 3.12: Phase surface for circular patch with exterior slots with 0.367λ inter-element spacing.

3.3.2 0.5λ Spacing

Given the insignificant effect of increasing the element spacing to 0.5λ in the previous sections, it is reasonable to expect that a similar result will occur here. Table 3.6 lists the simulation parameters.

The phase surface is nearly identical to the sub-wavelength spaced version, as seen in Figure 3.14. The same issue with long slot lengths and small patch radii is also present here in the left side of the graph. The phase range is 328 degrees. The slopes are roughly identical as well.

The magnitude of the reflection coefficient did not decrease as much as other designs

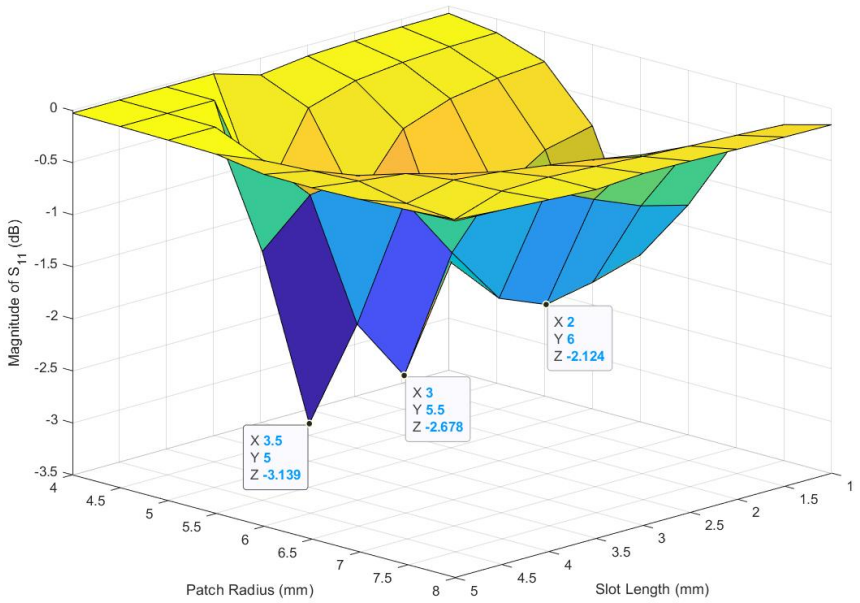

Figure 3.13: Magnitude surface for circular patch with exterior slots with 0.367λ inter-element spacing.

Table 3.6: Simulation parameters for 0.5λ spaced circular patch with exterior slots.

Substrate	Inter-Element Spacing	Slot Width	Patch Radius	Slot
FR-4, 3mm thick, ϵ_r =4.4	25.9mm (0.5λ)	1.5mm	4 to 8mm	1 to 5mm

when the inter-element spacing was increased. In Figure 3.15, the minimum magnitude is -3.8 dB, only down 0.7 dB from the smaller lattice size case. However, the resonance peaks themselves are wider, which is a minor disadvantage in terms of hologram accuracy compared to the sub-wavelength spaced lattice.

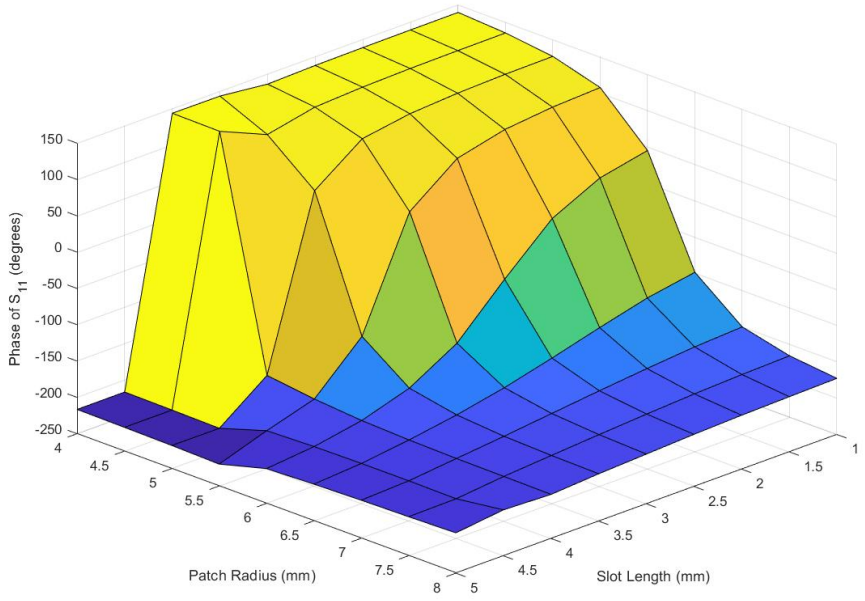

Figure 3.14: Phase surface for circular patch with exterior slots with 0.5λ inter-element spacing.

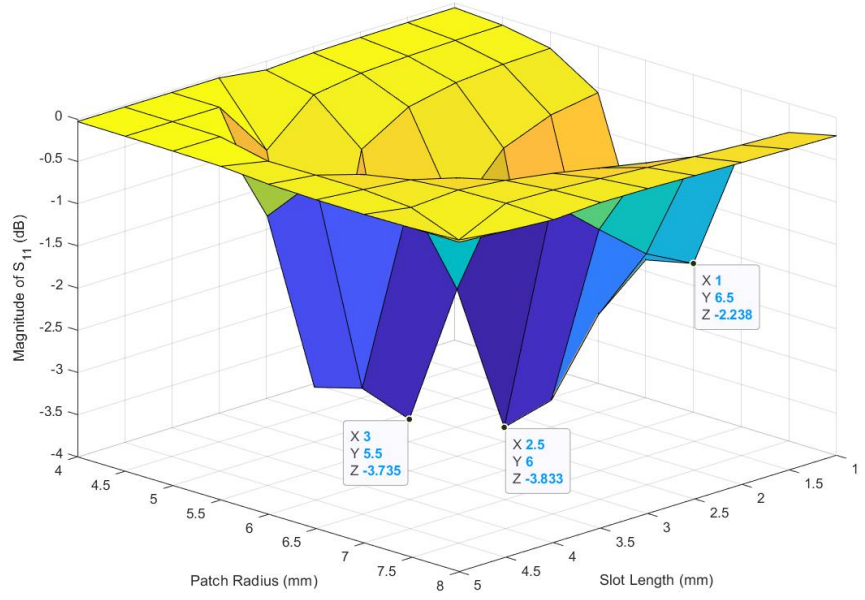

Figure 3.15: Magnitude surface for circular patch with exterior slots with 0.5λ inter-element spacing.

CHAPTER 4
PILOT SIGNAL DESIGN

In many studies of reflectarrays for wireless power transfer, the feed is assumed to be close to the reflectarray surface. This is a carryover from the use of reflectarrays in communications systems, where the reflectarray is used as essentially a one-to-one replacement for a parabolic dish. However, for a wireless power transfer reflectarray, this arrangement poses two primary problems.

First, wireless power transfer always has to compete with the ability to generate energy at the receiver site independently. The primary selling point of wireless power transfer is the ability to transfer much more power than can be feasibly generated at the receiver location. Therefore, long power links and high power are essential for wireless power transfer to compete with *in situ* power generation. However, a wireless power transfer system with a single or a small number of feeds would quickly run into problems with scale. If a single link requires, for example, 1 MW of power, then a single-feed reflectarray system would require the feed system to handle 1 MW of continuous power over presumably long-term conditions. This would require cutting-edge and expensive microwave sources and materials at best, and whole new technologies at worst. Even splitting the requirement up to 100 kW for multiple feeds would be far more expensive than 100 kW diesel generators or similar generation schemes at the receiver site.

Second, as the planar reflectarray grows larger, the radiation from a single or a small number of feeds is spread over a larger area. Visualizing each feed as a spherical wave from a point source, it is quickly evident that at larger parallel distances to the reflectarray surface, the angle of the incident radiation is further from the nominal feed angle that each reflectarray element was designed for. At angles of incident radiation closer to parallel, the performance of the reflectarray elements degrades [7].

The first issue may be addressed using spatial power combining. This is a concept in which reflectarray unit cells or groups of unit cells each contain a microwave power oscillator. This oscillator is phase locked to the incoming signal and adds power to the reflection in phase with the original reflected signal. Instead of combining the power in a transmission line network or waveguide, the power from each oscillator is radiated into space and the sum of the power from every microwave oscillator combines at the receiver. This allows the power of the system to be mostly tied to the area of the transmitting reflectarray instead of the technology of the microwave source. Adding power to the system simply requires that more array elements are added.

In effect, phase locking the oscillators in this way is the same as providing a reflection coefficient at the reflectarray surface that is greater than unity. In literature, a very similar concept is known as the reflection amplifier, often used in backscatter radio [38, 39, 40, 41, 42, 43, 44]. However, a reflection amplifier designed for intermittent communication has a non-oscillatory requirement, which requires bias points such that high power levels are not feasible[45].

In this configuration, a feed close to the reflectarray is not needed. The input pilot signal is only required to provide something for the oscillators to phase lock onto to radiate coherently. Therefore, the feeds can potentially be removed from the structure entirely. Instead, a single antenna pilot source can be used at the receiver. For a large beam distance, the low-power pilot signal from a single antenna resembles a plane wave. This arrangement is studied in Section 4.1.

A potential issue with the plane-wave pilot signal is that the oscillators require a certain level of input signal power for the phase locking to be successful. If the pilot signal source is a simple directional communications-type antenna, the pilot power level at the reflectarray surface could be too low for phase locking. However, if the receiver has to be large anyway for efficient wireless power transfer, it is feasible that the receiver could be used as a phased array to provide a large amount of pilot power to the transmitter. The transmitter would

then reflect that power back and add to it using the power oscillators, resulting in an overall power gain at the receiver. This system configuration is studied in Section 4.2.

4.1 Far-Field Plane Wave

In communications systems, transmitted radiation over a long-distance communications link is assumed to be a plane wave locally at the receiver. This assumption is good for a wireless power transfer pilot signal if the pilot signal antenna gain is relatively constant over the angular distance corresponding to the transmission aperture. As a quick grounding example, a Space Solar Power satellite in 36000km geostationary orbit might have a transmitting aperture of 4km in diameter. The angular size of the Space Solar Power satellite at the ground station would be around 0.006 degrees. The gain of the pilot signal beam is unlikely to change drastically over such a small angular distance, so the plane wave assumption holds well in this archetypal example of wireless power transfer.

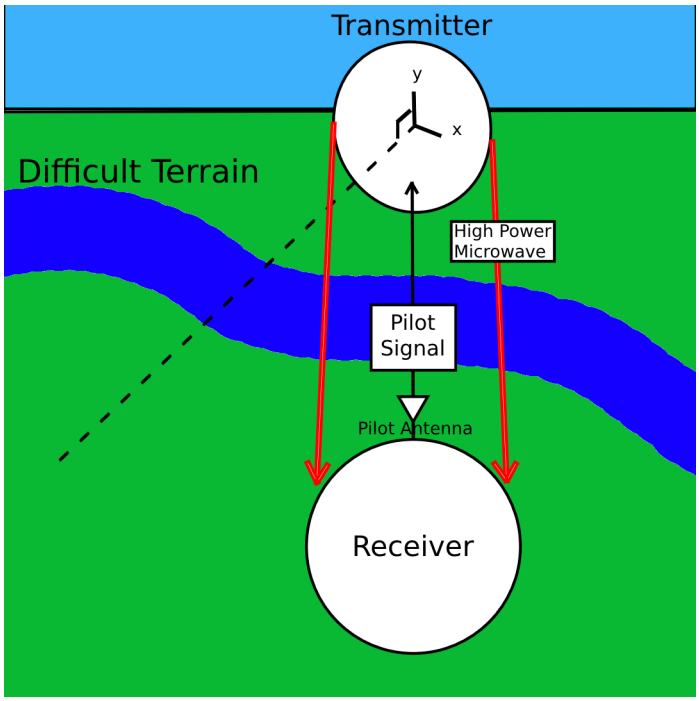

Figure 4.1: Example of a wireless power transfer system configuration using a far-field pilot signal.

The hypothetical wireless power transfer system in Figure 4.1 uses a far-field radiating

antenna at the receiver to illuminate the surface of the transmitter over a long distance over difficult terrain. The receiver and transmitter must be located within the radiative near field (Fresnel) region, lying between the reactive near field and far field (Frauenhofer) regions. For large apertures, the Fresnel region lies between $0.62\sqrt{\frac{D^3}{\lambda}}$ and $\frac{2D^2}{\lambda}$ [46].

As an example, the aperture diameter in this scenario is set at 4 meters for both transmit and receive. The Fresnel region would therefore span the down-range distance between 21.8 meters and 618.7 meters. Past 618.7 meters, the 4 meter aperture would no longer be able to create a focus spot. Using a significantly smaller pilot antenna, a pilot signal is transmitted from the receiver and illuminates the transmitting reflectarray. Since the transmitted power level is low, the low spillover efficiency is inconsequential. The phase of the wave incident on the surface of the transmit reflectarray at 10 degrees off-axis is shown in Figure 4.2.

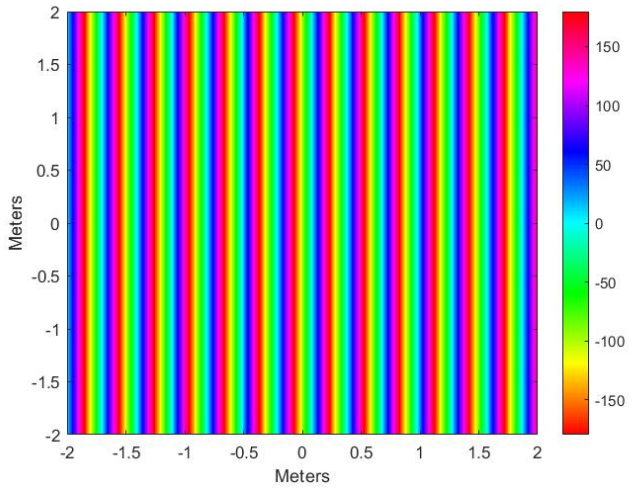

Figure 4.2: Phase of incident far-field pilot plane wave on the transmit reflectarray.

The magnitude distribution of the electric field across the transmit reflectarray surface is constant because of the plane wave assumption. This is beneficial due to the fact that the power oscillators will have a uniform level of input signal to phase lock to over the entire transmit reflectarray. Otherwise, the magnitude is much less important than the phase in terms of determining the focusing behavior [47].

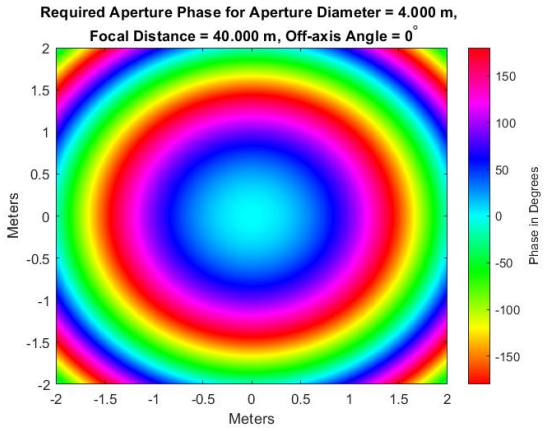

(a) Required phase for on-axis beam.

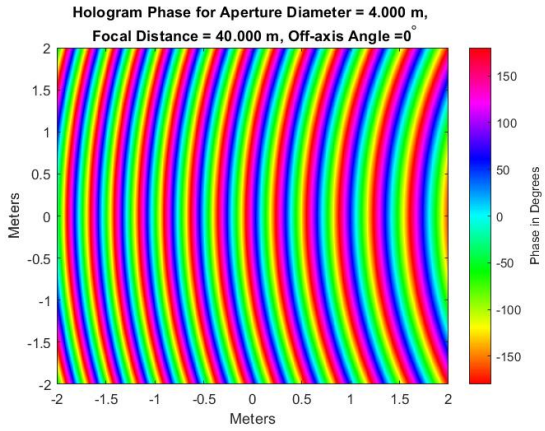

(b) Hologram for on-axis beam.

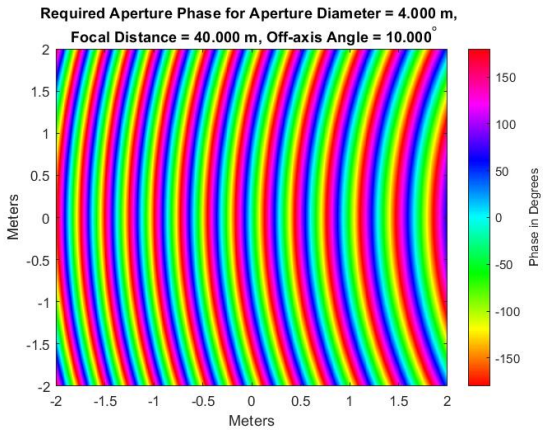

(c) Required phase for 10 degree off-axis beam.

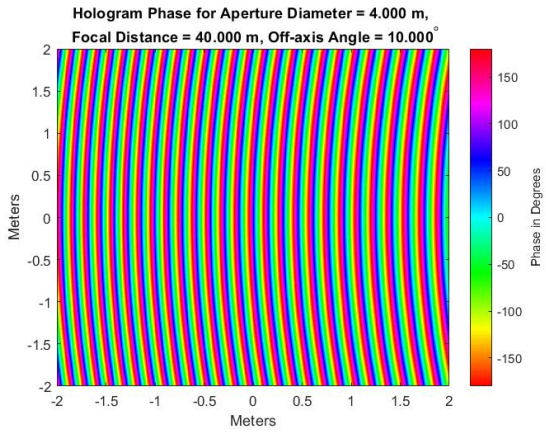

(d) Hologram for 10 degree off-axis beam.

Figure 4.3: Required phase distributions and hologram phases for far-field pilot signal.

Once the incident phase is known, the hologram phase can be calculated by interfering the desired surface phase from Equation (1.1) with the incident phase. In other words,

$$\Phi_{incident} + \Phi_{hologram} = \Phi_{desired\_surface} \tag{4.1}$$

$$\Phi_{hologram} = \Phi_{desired\_surface} - \Phi_{incident} \tag{4.2}$$

Figure 4.3 shows the desired surface phase on the left to produce the focus spot and the hologram result on the right for on-axis power transfer and 10 degrees off-axis power transfer. The hologram phases on the right can be used with the phase plots in Chapter 3 to generate a full physical reflectarray. However, without active power oscillators on the

reflectarray, this wireless power transfer scheme lacks utility, as the pilot power originates from the receiver to begin with.

4.2 Fresnel Zone Focusing

Phase locking to a reference signal requires error detection between a feedback signal and the reference signal. However, error detectors require that the reference signal is above some threshold for optimal performance. In a far-field pilot signal scenario, it is possible that the power delivered to the phase lock loop error detectors is not sufficient to provide a clean reference signal and lock the output phase of the power oscillators. An alternative to a far-field pilot signal that would satisfy the reference signal power requirement could be a Fresnel-zone focused pilot signal. This system configuration is shown in Figure 4.4.

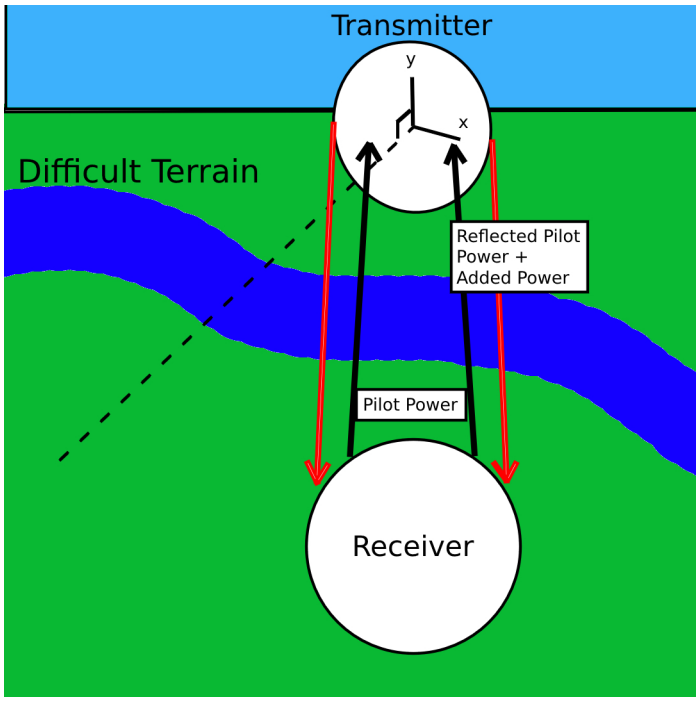

Figure 4.4: Example of a wireless power transfer system configuration using a Fresnel focused pilot signal.

In this configuration, a larger amount of power is delivered from the receiver to the transmitter via a Fresnel-focused pilot signal. It has been demonstrated in the literature

that the transmitted electric field can be accurately described as a Gaussian beam in this scenario [47]. The following simulation builds on the results of [47].

The electric field of a Gaussian beam can be described analytically as [6][48]:

$$\frac{E(x,y,z)}{E_0} = \frac{w_0}{w(z)} \exp\left(-\frac{r^2}{w(z)^2}\right) \exp\left(-j\frac{\beta r^2}{2R(z)}\right) \exp\Big(-j(\beta z - \phi(z))\Big) \tag{4.3}$$

$$w_0 = \frac{4}{\pi} \frac{z_0 \lambda_0}{D \cos^2(\theta)} \tag{4.4}$$

$$z_R = \frac{\pi w_0^2}{\lambda_0} \tag{4.5}$$

$$w(z) = w_0 \sqrt{1 + \left(\frac{z}{z_R}\right)^2} \tag{4.6}$$

$$R(z) = z\left(1 + \frac{z_R^2}{z^2}\right) \tag{4.7}$$

$$\phi(z) = \tan^{-1}\left(\frac{z}{z_R}\right) \tag{4.8}$$

$$r = \sqrt{x^2 + y^2} \tag{4.9}$$

w_0 : Minimum beam waist

z_R : Rayleigh length

$w(z)$: Beam waist

$R(z)$: Radius of curvature

$\phi(z)$: Guoy phase shift

θ : Angle between normal of the aperture and the vector defined from the center of aperture to focus

To generate the required hologram, the above equations must be used to first generate the incident wave on the reflectarray surface. No quantization error from the receiver phased array is included in the analysis. Since a 4 meter transmit antenna is used, the minimum waist size w_0 is set to 3 meters to capture over 90% of the pilot energy transmitted from the receiver [47]. The angle of incidence θ is then set to 10 degrees off-axis. From w_0 and θ, the on-axis focal distance is calculated by setting $w(z)$=w_0 and solving for z. The Rayleigh distance z_R is also calculated.

Then, for every point on the transmit aperture (which is not perpendicular to the principle axis of radiation), $R(z)$, r, $w(z)$, and $\phi(z)$ are calculated. This is done by converting the coordinate system of the transmit aperture (x, y, z) to the coordinate system of the beam (x', y', z') using the relations:

$$\cos\theta = \frac{x}{x'}$$

$$y = y'$$

$$\tan\theta = \frac{z'}{x'}$$

and calculating the electric field complex phasor at each point (x, y, F) on the transmit aperture. This results in the plots shown in Figure 4.5. The calculated focal distance is 555.6 meters, which still lies safely within the Fresnel focus zone.

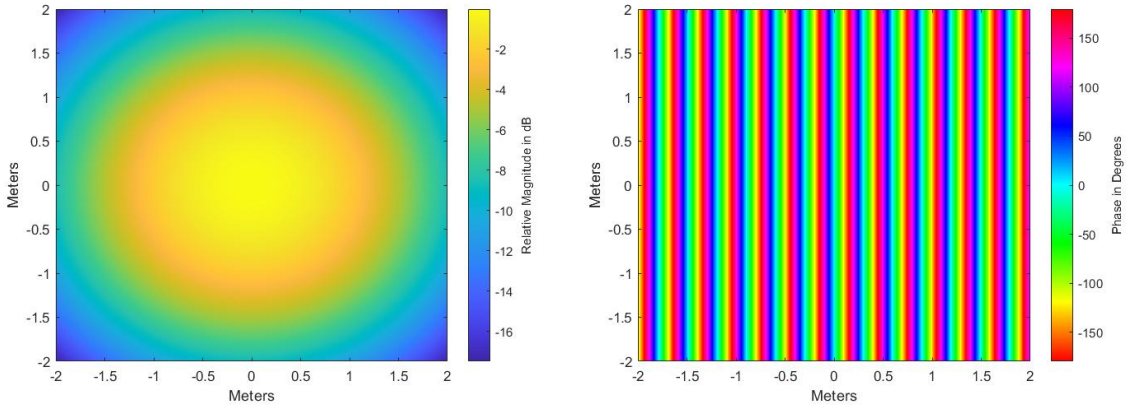

(a) Magnitude of Fresnel focused pilot signal (b) Phase of Fresnel focused pilot signal

Figure 4.5: Electric field distribution of Fresnel-focused pilot signal on the transmit aperture at 10 degrees off-axis and 556 meters focal distance.

Figure 4.5a shows the magnitude distribution of the incident electric field in dB, normalized to the electric field magnitude at the origin of the Gaussian beam. It shows that the majority of the energy in the beam is contained within the transmit aperture. Since the off-axis angle is small, the skew of the focus spot is not clear, but is more pronounced in higher off-axis angles. However, as established in [7] higher off-axis angles perform worse in general, so high power wireless power transfer systems will most likely use low (closer to normal) off-axis angles.

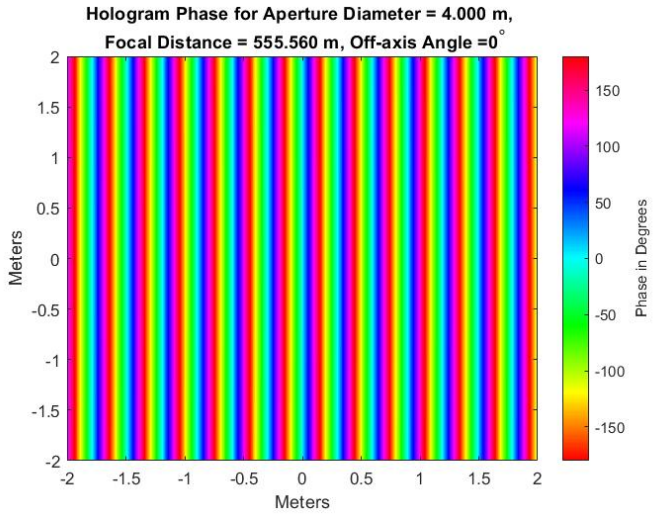

Figure 4.6: Hologram phase for on-axis Fresnel-focused pilot signal.

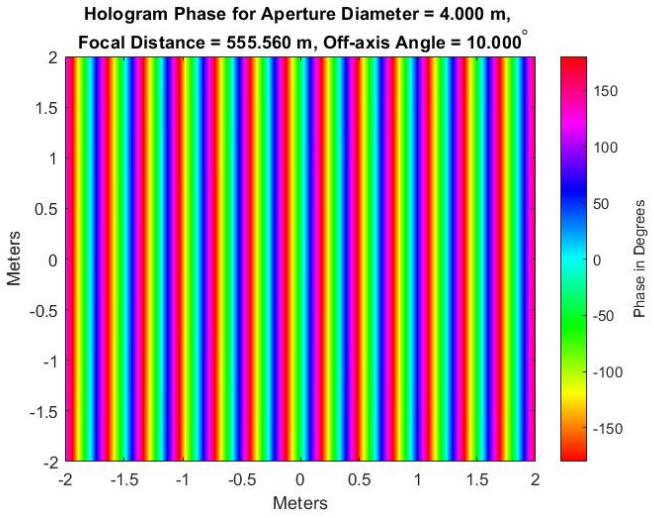

Figure 4.7: Hologram phase for 10 degree off-axis Fresnel-focused pilot signal.

Figure 4.5b shows that the incident phase of the Fresnel focused pilot beam is actually extremely similar to the incident phase of the far-field pilot signal. As such, the hologram phases for both on-axis and 10 degree off-axis radiation (Figure 4.6 and Figure 4.7) are very similar to the holograms in Section 4.1. While the focal distance in Section 4.1 is much smaller, Figure 4.8 plots the difference in phase distribution for the hologram phase focusing at the same distance as Figure 4.7 using a far-field pilot signal. The phase distributions are slightly shifted and are not identical.

Figure 4.8: Difference in hologram phases for far-field pilot signal and Fresnel-focused pilot signal at 10 degrees off-axis radiation and 555.6m focal distance.

CHAPTER 5
CONCLUSION

5.1 Discussion of Results

In this work, several aspects of large-scale wireless power transfer systems using holographic reflectarrays are investigated at 5.8 GHz. These include hexagonal reflectarray unit cells, modified circular patch elements, and different types of retrodirective pilot signals.

Hexagonal unit cells provide better packing efficiency and provide uniform inter-element spacing throughout the whole array. While the phase response of the circular reflectarray patches was not altered greatly, the magnitude of the reflection response was higher in all cases for the same inter-element spacing as the square unit cell from [7]. In addition, the result from [7] that a thicker substrate increases the bandwidth and decreases the phase slope of a reflectarray element is confirmed.

Three variations of the simple circular patch element from literature are simulated to find a reflectarray element with more degrees of freedom in phase tuning and to increase mechanical tolerances. The cross slot and exterior slot loaded circular patches showed low phase slopes and adequate phase ranges, and can successfully replace the circular patch in a reflectarray design. The high phase slope of the ring slot loaded circular patch and the low bandwidth with respect to patch radius make it a poor candidate for a reflectarray element compared to the other two.

Finally, as high-power wireless power transfer systems using reflectarrays are more likely to use spatial power combining of power oscillators, it is more practical to remove the feed from the transmit reflectarray entirely and use the receiver as a feed to provide a phase reference to the power oscillators at the transmit reflectarray. This can be done by means of a far-field plane wave generated using a standard small antenna or using the

whole receiver aperture (assuming similar transmit and receive aperture sizes) to generate a Fresnel-focused pilot signal incident on the transmitter aperture. It is found that the transmit reflectarray hologram does not change significantly, meaning that the Fresnel-focused pilot signal is a viable choice if higher feed power is required for phase locking of the power oscillators.

5.2 Future Work

5.2.1 Further Substrate Investigation

In this study, the substrates were assumed to be homogeneous and isotropic. While this is a fairly good assumption for Rogers RO4003C, the FR-4 used for the majority of the simulations often differs from this ideal significantly. Feasibility studies on the level of focusing achievable with varying levels of inhomogeneity and anisotropy should be performed in the context of very large transmit and receive areas.

If the holographic reflectarray is viewed as an artificial impedance surface, changing the substrate thickness and dielectric constant will influence the equivalent complex impedance per area of the surface and therefore change the bandwidth and resonant frequency of the reflectarray elements [11]. Further work is needed to understand these effects so they can be balanced against substrate cost.

Finally, since the structures involved will be handling high levels of microwave power, thermal studies should be performed for a transmitting reflectarray to investigate how thermal effects will influence the focusing behavior of the reflectarray. For large reflectarrays, mechanical warping of the surface may become pronounced over the large surface areas. Additionally, the substrate electrical parameters, including loss and dielectric constant, may not be invariant over temperature, especially with low cost substrates.

5.2.2 Further Array Element Design

The reflectarray elements investigated in this study are by no means the only possible elements for a wireless power transfer system. There exist infinite configurations of conductor geometry in a unit cell to create reflectarray elements, from simple and well-studied [18] to new fractal elements[49]. Analysis of other reflectarray element types would benefit a future wireless power transfer system design.

In addition, more detailed statistical analysis can be performed on each reflectarray element type to determine the geometries least sensitive to manufacturing error. This can be performed using either Monte Carlo simulations or taking numerical derivatives of key physical parameters, both of which are supported by the Ansys HFSS software.

5.2.3 Phase-locked Power Oscillators

As mentioned before, power oscillators distributed across the transmit reflectarray and phase-locked to the pilot signal are essential to the operation of reflectarray-based large scale wireless power transfer systems, especially if transmitter-side feeds are removed from the design. Gallium nitride high electron mobility transistors (GaN HEMTs) are a promising technology that offer high efficiency and power at microwave frequencies. In particular, [50] has developed a straightforward design procedure for GaN power oscillators used in [51] to design oscillators up to 58.4% percent efficiency at 38 dBm output power.

However, the entire phase lock circuit requires more careful analysis. The literature regarding phase locked loops is extensive but complex, and care must be taken during the selection of the feedback loop and phase detector so that the output phase of the oscillator is in phase with the reflected signal. Since the Gabor hologram method is a phase-based technique, phase error introduced by the phase locked loop may significantly detrimentally affect the total hologram phase and therefore the power at the receiver. The oscillator in [51] could also require modification for use in this system. Development of the phase locked power oscillator is a key step in developing feasible large-scale wireless power transfer

systems, so this is a critical next step for further research.

5.2.4 Active Beam Steering

Adding phase shifters into reflectarray elements for beam steering is an active area of ongoing research. There are several principal methods of phase tuning that could be applicable to reflectarray element phase tuning. One uses the bias level of varactors to change the load impedance of each reflectarray element, thereby changing the resonant frequency[52][53]. Another uses RF PIN or MEMS diodes to change the effective length of slots in the microstrip patch, which also changes the resonant frequency of the patch[54][55]. Still others that are less applicable to reflectarrays physically move the feed[56][57] or dielectric height[58]. While the first option provides more granular phase control, the second is particularly useful for reflectarray elements such as the circular patch loaded with a cross slot from Section 3.1.

While beam steering could be an attractive feature for a wireless power transfer system so that multiple receivers can be serviced, it is not an enabling technology in the same way that embedded phase-locked power oscillators would be. A full demonstration can be constructed using a transmitting reflectarray without needing beam steering capability. In a full scale wireless power transfer where the receiver moves very rarely, it is possible that the steering could be performed entirely mechanically at a lower cost by rotating the reflectarray. However, this feature would be necessary for wireless power transfer in highly asymmetric mobile scenarios, e.g. powering airborne drones or satellites [59][6].

5.2.5 Receiver Station Design

While many high-efficiency rectifying antenna designs exist in the literature [60], these designs often only consider cost at a high level or not at all. Therefore, further receiver station development taking cost into account is still required for a real large-scale implementation. In addition, receivers capable of simultaneous transmission of a Fresnel-focused pilot sig-

nal and reception of the corresponding high power Gaussian beam from the transmitter have not been the subject of any study that the current author is aware of. More development and investigation of this large-scale wireless power transfer paradigm is required.

A potential system configuration that could be useful in some scenarios is that of bistatic power transfer, in which the pilot signal originates from a point other than the receiver. If the receiver location cannot generate enough energy for the pilot signal, then a separate location could generate the Fresnel focused pilot signal and the hologram phase can direct the reflected and added power to the final receiver location.

5.2.6 Fabrication and Test

Finally, the results presented in this work have not been used to design and simulate a full reflectarray. Since the principles of operation are identical to those of reflectarrays in the literature, showing the theoretical performance of a full reflectarray would still be highly useful. The next steps would then be to manufacture a full holographic reflectarray. However, since it is a Fresnel zone device, characterizing the behavior of the beam would be difficult. For a better idea of system performance, a full scaled-down wireless power transfer demonstration would have to be prepared, including the development of a receiver aperture with combined rectifying antennas and transmitting antennas for the pilot signal. The ultimate culmination of this line of research is to include power oscillators in the transmit reflectarray and create a full scaled-down wireless power transfer demonstration.

Appendices

APPENDIX A

MATLAB CODE

```
% ffpilot.m
% Investigating phase distribution on transmit aperture using far field
% plane wave pilot signal.
% Written by Evan Shi for MSECE thesis @ Georgia Institute of Technology

freq = 5.8e9; % Hz
c= physconst('LightSpeed');
lambda = c/freq;
beta = (2*pi)/lambda;

% Angle of incidence (relative to normal to reflectarray) of the receiver
angleIncidence = 0; % degrees
kz = cosd(angleIncidence);
kx = sind(angleIncidence);

%F = 40; % Focal distance (m)
D = 4; % diameter of aperture, m
numPoints = 1000;
incidentMatrix = ones(numPoints,numPoints);
pixelSize = D/numPoints;
```

```
21
22 for iterator = 1:numPoints
23     for jterator = 1:numPoints
24         incidentMatrix(iterator,jterator) = beta*(kx*(
               jterator*pixelSize));
25     end
26 end
27 A = pixelSize/2;
28 x = floor(-numPoints/2)*pixelSize+A:pixelSize:floor(
   numPoints/2)*pixelSize-A;
29 y = floor(numPoints/2)*pixelSize-A:-pixelSize:floor(-
   numPoints/2)*pixelSize+A;
30 figure;
31 incidentMatrix = rad2deg(incidentMatrix);
32 incidentMatrix = wrapTo180(incidentMatrix);
33 imagesc(x,y,incidentMatrix);
34 xlabel('Meters');
35 ylabel('Meters');
36 colormap(hsv);
37 h = colorbar;
38 set(gca,'YDir','normal') %Make the y axis go from - to +
39
40 normalMatrix = zeros(numPoints,numPoints);
41 % Calculate required phase at pixel for on-axis radiation
42 for r = 1:numPoints
43     for c = 1:numPoints
```

```
44          normalMatrix(r,c) = (2*pi/lambda)*(sqrt(x(c).^2 + y(
               r).^2 + F^2)-F);
45      end
46  end
47
48  figure
49  normalMatrix= rad2deg(normalMatrix);
50  normalMatrix = wrapTo180(normalMatrix);
51  imagesc(x,y,normalMatrix);
52  xlabel('Meters');
53  ylabel('Meters');
54  colormap(hsv);
55  h = colorbar;
56  ylabel(h,'Phase in Degrees');
57  title(sprintf('Required Aperture Phase for Aperture Diameter
        = %0.3f m, \n Focal Distance = %0.3f m, Off-axis Angle =
        0^\\circ',D, F));
58  set(gca,'YDir','normal') %Make the y axis go from - to +
59
60  % Calculate phase at pixel for skewed radiation
61  angleMatrix = zeros(numPoints,numPoints);
62  x0 = F*tand(angleIncidence);
63  for r = 1:numPoints
64      for c = 1:numPoints
65          angleMatrix(r,c) = (2*pi/lambda)*(sqrt((x(c)-x0).^2
               + y(r).^2 + F^2)-F);
66      end
```

```
67 end
68
69
70 figure
71 angleMatrix = rad2deg(angleMatrix);
72 angleMatrix = wrapTo180(angleMatrix);
73 imagesc(x,y,angleMatrix);
74 xlabel('Meters');
75 ylabel('Meters');
76 colormap(hsv);
77 h = colorbar;
78 ylabel(h,'Phase in Degrees');
79 title(sprintf('Required Aperture Phase for Aperture Diameter
       = %0.3f m, \n Focal Distance = %0.3f m, Off-axis Angle =
       %0.3f^\\circ',D, F,angleIncidence));
80 set(gca,'YDir','normal') %Make the y axis go from - to +
81
82
83 % Calculate hologram
84 % Normal matrix
85 holoNormal = normalMatrix - incidentMatrix;
86 figure
87 holoNormal = wrapTo180(holoNormal);
88 imagesc(x,y,holoNormal);
89 xlabel('Meters');
90 ylabel('Meters');
91 colormap(hsv);
```

```
92 h = colorbar;
93 ylabel(h,'Phase in Degrees');
94 title(sprintf('Hologram Phase for Aperture Diameter = %0.3f
      m, \n Focal Distance = %0.3f m, Off-axis Angle =0^\\circ'
      ,D, F));
95 set(gca,'YDir','normal') %Make the y axis go from - to +
96
97 % Calculate hologram
98 % Angled matrix
99 holoAngle = angleMatrix - incidentMatrix;
100 figure
101 holoAngle = wrapTo180(holoAngle);
102 imagesc(x,y,holoAngle);
103 xlabel('Meters');
104 ylabel('Meters');
105 colormap(hsv);
106 h = colorbar;
107 ylabel(h,'Phase in Degrees');
108 title(sprintf('Hologram Phase for Aperture Diameter = %0.3f
      m, \n Focal Distance = %0.3f m, Off-axis Angle = %0.3f^\\
      circ',D, F,angleIncidence));
109 set(gca,'YDir','normal') %Make the y axis go from - to +
```

```
1 % fresnelpilot.m
2 % Investigating phase distribution on transmit aperture
      using Fresnel
3 % focused pilot signal.
```

```
4  % Written by Evan Shi for MSECE thesis @ Georgia Institute
       of Technology
5
6  freq = 5.8e9; % Hz
7  c= physconst('LightSpeed');
8  lambda = c/freq;
9  beta = (2*pi)/lambda;
10
11 % Angle of incidence (relative to normal to reflectarray) of
       the receiver
12 angleIncidence = 10; % degrees
13
14 D = 4; % diameter of aperture, m
15 numPoints = 1000;
16 incidentMatrix = ones(numPoints,numPoints);
17 pixelSize = D/numPoints;
18
19 % Gaussian beam characteristics
20 w0 = 3;
21 F = w0 /((4/pi)*((lambda)/(pi*D*(cosd(angleIncidence)^2))));
22 Zr = (pi*w0^2)/lambda;
23
24 A = pixelSize/2;
25 x = floor(-numPoints/2)*pixelSize+A:pixelSize:floor(
       numPoints/2)*pixelSize-A;
26 y = floor(numPoints/2)*pixelSize-A:-pixelSize:floor(-
       numPoints/2)*pixelSize+A;
```

```
27
28 for iterator = 1:numPoints
29     for jterator = 1:numPoints
30         xprime = x(jterator)*cosd(angleIncidence);
31         zprime = xprime * tand(angleIncidence);
32         r = sqrt(xprime^2 + y(iterator)^2);
33         wz = 3*sqrt(1+(zprime/Zr)^2);
34         phiz = atan(zprime/Zr);
35         Rz = F*(1+(Zr/zprime)^2);
36         incidentMatrix(iterator,jterator) = (w0/wz)*exp(-r
               ^2/wz^2)*exp((1i*beta*r^2)/(2*Rz))*exp(-1i*(beta*
               zprime)-phiz);
37     end
38 end
39
40
41 figure;
42 incidentMatrixPhase = angle(incidentMatrix);
43 incidentMatrixPhase = rad2deg(incidentMatrixPhase);
44 incidentMatrixPhase = wrapTo180(incidentMatrixPhase);
45 imagesc(x,y,incidentMatrixPhase);
46 xlabel('Meters');
47 ylabel('Meters');
48 colormap(hsv);
49 h = colorbar;
50 ylabel(h,'Phase in Degrees');
51 set(gca,'YDir','normal') %Make the y axis go from - to +
```

```
52
53 figure;
54 imagesc(x,y,20*log(abs(incidentMatrix)));
55 xlabel('Meters');
56 ylabel('Meters');
57 %colormap(hsv);
58 h = colorbar;
59 ylabel(h,'Relative Magnitude in dB');
60 set(gca,'YDir','normal') %Make the y axis go from - to +
61
62
63 normalMatrix = zeros(numPoints,numPoints);
64 % Calculate required phase at pixel for on-axis radiation
65 for r = 1:numPoints
66     for c = 1:numPoints
67         normalMatrix(r,c) = (2*pi/lambda)*(sqrt(x(c).^2 + y(
              r).^2 + F^2)-F);
68     end
69 end
70
71 % figure
72 % normalMatrix= rad2deg(normalMatrix);
73 % normalMatrix = wrapTo180(normalMatrix);
74 % imagesc(x,y,normalMatrix);
75 % xlabel('Meters');
76 % ylabel('Meters');
77 % colormap(hsv);
```

```
% h = colorbar;
% ylabel(h,'Phase in Degrees');
% title(sprintf('Required Aperture Phase for Aperture
   Diameter = %0.3f m, \n Focal Distance = %0.3f m, Off-axis
    Angle = 0^\\circ',D, F));
% set(gca,'YDir','normal') %Make the y axis go from - to +

% Calculate phase at pixel for skewed radiation
angleMatrix = zeros(numPoints,numPoints);
x0 = F*tand(angleIncidence);
for r = 1:numPoints
    for c = 1:numPoints
        angleMatrix(r,c) = (2*pi/lambda)*(sqrt((x(c)-x0).^2
           + y(r).^2 + F^2)-F);
    end
end

%
% figure
% angleMatrix = rad2deg(angleMatrix);
% angleMatrix = wrapTo180(angleMatrix);
% imagesc(x,y,angleMatrix);
% xlabel('Meters');
% ylabel('Meters');
% colormap(hsv);
% h = colorbar;
% ylabel(h,'Phase in Degrees');
```

```
102 % title(sprintf('Required Aperture Phase for Aperture
       Diameter = %0.3f m, \n Focal Distance = %0.3f m, Off-axis
        Angle = %0.3f^\\circ',D, F,angle));
103 % set(gca,'YDir','normal') %Make the y axis go from - to +
104
105
106 % Calculate hologram
107 % Normal matrix
108 holoNormal = normalMatrix - incidentMatrixPhase ;
109 figure
110 holoNormal = wrapTo180(holoNormal);
111 imagesc(x,y,holoNormal);
112 xlabel('Meters');
113 ylabel('Meters');
114 colormap(hsv);
115 h = colorbar;
116 ylabel(h,'Phase in Degrees');
117 title(sprintf('Hologram Phase for Aperture Diameter = %0.3f
       m, \n Focal Distance = %0.3f m, Off-axis Angle =0^\\circ'
       ,D, F));
118 set(gca,'YDir','normal') %Make the y axis go from - to +
119
120 % Calculate hologram
121 % Angled matrix
122 holoAngle1 = angleMatrix - incidentMatrixPhase ;
123 figure
124 holoAngle1 = wrapTo180(holoAngle1);
```

```
125 imagesc(x,y,holoAngle1);
126 xlabel('Meters');
127 ylabel('Meters');
128 colormap(hsv);
129 h = colorbar;
130 ylabel(h,'Phase in Degrees');
131 title(sprintf('Hologram Phase for Aperture Diameter = %0.3f
       m, \n Focal Distance = %0.3f m, Off-axis Angle = %0.3f^\\
       circ',D, F,angleIncidence));
132 set(gca,'YDir','normal') %Make the y axis go from - to +
133
134
135 % diffHolo = holoAngle - holoAngle1;
136 % figure
137 % diffHolo= wrapTo180(diffHolo);
138 % imagesc(x,y,diffHolo);
139 % xlabel('Meters');
140 % ylabel('Meters');
141 % colormap(hsv);
142 % h = colorbar;
143 % ylabel(h,'Phase in Degrees');
144 % title(sprintf('Difference in Hologram Phase for Aperture
       Diameter = %0.3f m, \n Focal Distance = %0.3f m, Off-axis
        Angle = %0.3f^\\circ',D, F,angleIncidence));
145 % set(gca,'YDir','normal') %Make the y axis go from - to +
```

REFERENCES

[1] X. Lu, P. Wang, D. Niyato, D. I. Kim, and Z. Han, "Wireless charging technologies: Fundamentals, standards, and network applications," *IEEE Communications Surveys Tutorials*, vol. 18, no. 2, pp. 1413–1452, 2016.

[2] C. H. Lee, G. Jung, K. A. Hosani, B. Song, D.-k. Seo, and D. Cho, "Wireless power transfer system for an autonomous electric vehicle," in *2020 IEEE Wireless Power Transfer Conference (WPTC)*, 2020, pp. 467–470.

[3] C. T. Rodenbeck, P. I. Jaffe, B. H. Strassner II, P. E. Hausgen, J. O. McSpadden, H. Kazemi, N. Shinohara, B. B. Tierney, C. B. DePuma, and A. P. Self, "Microwave and millimeter wave power beaming," *IEEE Journal of Microwaves*, vol. 1, no. 1, pp. 229–259, 2021.

[4] "Attenuation by atmospheric gases," ITU-R, World Bank Policy Research Working Paper Recommendation ITU-R P.676-10, 2013.

[5] "Ieee standard for definitions of terms for antennas," *IEEE Std 145-2013 (Revision of IEEE Std 145-1993)*, pp. 1–50, 2014.

[6] W. Brown and E. Eves, "Beamed microwave power transmission and its application to space," *IEEE Transactions on Microwave Theory and Techniques*, vol. 40, no. 6, pp. 1239–1250, 1992.

[7] E. Backer, "Holographic transmit reflect array at 5.8 ghz for wireless power transfer in the fresnel zone," M.S. thesis, Georgia Institute of Technology, 2019.

[8] E. Backer, M. Alhassoun, and G. D. Durgin, "Design of a circular-patch reflectarray for microwave power transfer and communications in space," in *2019 IEEE International Conference on Wireless for Space and Extreme Environments (WiSEE)*, 2019, pp. 93–98.

[9] J. Huang, "Microstrip reflectarray," in *Antennas and Propagation Society Symposium 1991 Digest*, 1991, 612–615 vol.2.

[10] D. Berry, R. Malech, and W. Kennedy, "The reflectarray antenna," *IEEE Transactions on Antennas and Propagation*, vol. 11, no. 6, pp. 645–651, 1963.

[11] D. Sievenpiper, J. Schaffner, H. Song, R. Loo, and G. Tangonan, "Two-dimensional beam steering using an electrically tunable impedance surface," *IEEE Transactions on Antennas and Propagation*, vol. 51, no. 10, pp. 2713–2722, 2003.

[12] J. Zhang, X. Ge, J. Zhang, J. He, Y. Fan, Z. Li, Z. Jin, L. Gao, J. Ling, and Z. Qi, "Research activities on high-power microwave sources in national university of defense technology of china," in *2015 IEEE Pulsed Power Conference (PPC)*, 2015, pp. 1–20.

[13] G. S. Lipworth, J. A. Hagerty, D. Arnitz, Y. A. Urzhumov, D. R. Nash, R. J. Hannigan, C. T. Tegreene, and M. S. Reynolds, "A large planar holographic reflectarray for fresnel-zone microwave wireless power transfer at 5.8 ghz," in *2018 IEEE/MTT-S International Microwave Symposium - IMS*, 2018, pp. 964–967.

[14] C. Rodenbeck, M.-y. Li, and K. Chang, "A phased-array architecture for retrodirective microwave power transmission from the space solar power satellite," in *2004 IEEE MTT-S International Microwave Symposium Digest (IEEE Cat. No.04CH37535)*, vol. 3, 2004, 1679–1682 Vol.3.

[15] Y. Dong, S.-w. Dong, Y. Wang, and L. Gong, "Calibration method of retrodirective antenna array for microwave power transmission," in *2013 IEEE Wireless Power Transfer (WPT)*, 2013, pp. 41–43.

[16] K.-i. Maki, M. Takahashi, K. Miyashiro, K. Tanaka, S. Sasaki, K. Kawahara, Y. Kamata, and K. Komurasaki, "Microwave characteristics of a wireless power transmission panel toward the orbital experiment of a solar power satellite," in *2012 IEEE MTT-S International Microwave Workshop Series on Innovative Wireless Power Transmission: Technologies, Systems, and Applications*, 2012, pp. 131–134.

[17] D. Gabor, "A new microscopic principle," *Nature*, vol. 161, pp. 777–778, 1948.

[18] P. Nayeri, F. Yang, and A. Z. Elserbeni, *Reflectarray Antennas: Theory, Designs, and Applications*. John Wiley and Sons, Inc., 2018.

[19] J. Huang and J. A. Encinar, *REFLECTARRAY ANTENNAS*. John Wiley and Sons, Inc., 2008.

[20] D. Pozar, S. Targonski, and H. Syrigos, "Design of millimeter wave microstrip reflectarrays," *IEEE Transactions on Antennas and Propagation*, vol. 45, no. 2, pp. 287–296, 1997.

[21] W. Yerazunis, B. Wang, and K. H. Teo, "Metamaterials and resonant array wireless power systems," in *2014 IEEE Antennas and Propagation Society International Symposium (APSURSI)*, 2014, pp. 1403–1404.

[22] O. Kiris, K. Topalli, and M. Unlu, "A reflectarray antenna using hexagonal lattice with enhanced beam steering capability," *IEEE Access*, vol. 7, pp. 45 526–45 532, 2019.

[23] M. D. Gregory, J. D. Binion, D. Z. Zhu, J. A. Easum, P. L. Werner, D. H. Werner, C. P. Scarborough, S. Griffiths, and J. P. Joint, "High power metasurface reflectarray antennas using switched shorted circular elements," in *2017 IEEE International Symposium on Antennas and Propagation USNC/URSI National Radio Science Meeting*, 2017, pp. 1037–1038.

[24] *Ansys Lecture 9: Unit Cell Analysis (Infinite Array)*, http://www.ece.uprm.edu/~rafaelr/inel6068/HFSS/HFSS_Antenna_v2015_v1/lectures_trainee/ANSYS_HFSS_Antenna_L09_0_Unit_Cell.pdf.

[25] *Ansys Workshop 9-1: Unit Cell Analysis (Infinite Array)*, http://www.ece.uprm.edu/~rafaelr/inel6068/HFSS/HFSS_Antenna_v2015_v1/workshop_instructions_trainee/ANSYS_HFSS_Antenna_W09_1_Unit_Cell.pdf.

[26] *Ansys Getting Started with HFSS Floquet Ports*, http://www.ece.uprm.edu/~rafaelr/inel6068/HFSS/GSG_HFSS_Floquet_Ports.pdf.

[27] *About Trace Width and Tolerance*, https://www.allpcb.com/pcb_trace_width_tolerance.html.

[28] *FR4 double sided copper coated board pcb laminate FR4 CCL copper clad laminate*, https://www.alibaba.com/product-detail/FR4-double-sided-copper-coated-board_60732898396.html?spm=a2700.pc_countrysearch.main07.3.4dd661d6HpPqQ8.

[29] *Double side laminate with polyester/ceramic dielectric*, https://www.rf-microwave.com/en/rogers-corp/ro4003c-0320-1e-1e/double-side-laminate-with-polyester-ceramic/ro4003-32-1-457x305/.

[30] M. H. Dahri, M. H. Jamaluddin, F. C. Seman, M. I. Abbasi, N. F. Sallehuddin, A. Y. I. Ashyap, and M. R. Kamarudin, "Aspects of efficiency enhancement in reflectarrays with analytical investigation and accurate measurement," *MDPI Electronics*, vol. 9, no. 11, 2020.

[31] H. Iwasaki, "A circularly polarized small-size microstrip antenna with a cross slot," *IEEE Transactions on Antennas and Propagation*, vol. 44, no. 10, pp. 1399–1401, 1996.

[32] A. K. Singh, R. K. Gangwar, and B. K. Kanaujia, "Cavity backed annular ring microstrip antenna loaded with concentric circular patch," in *The 8th European Conference on Antennas and Propagation (EuCAP 2014)*, 2014, pp. 2155–2158.

[33] S. Gao, L. Ge, D. Zhang, and W. Qin, "Low-profile dual-band stacked microstrip monopolar patch antenna for wlan and car-to-car communications," *IEEE Access*, vol. 6, pp. 69 575–69 581, 2018.

[34] A. Al-Zoubi, F. Yang, and A. Kishk, "A broadband center-fed circular patch-ring antenna with a monopole like radiation pattern," *IEEE Transactions on Antennas and Propagation*, vol. 57, no. 3, pp. 789–792, 2009.

[35] K.-L. Wong, *Compact and Broadband Microstrip Antennas*. John Wiley and Sons, Inc., 2002.

[36] J. Yu, Y. Sun, H. Fang, and F. Li, "A novel stacked patch antenna with dual band and diverse pattern characteristics," *Microwave and Optical Technology Letters*, vol. 62, no. 1, pp. 453–465, 2020. eprint: https://onlinelibrary.wiley.com/doi/pdf/10.1002/mop.32036.

[37] K. M. Mak, H. W. Lai, K. M. Luk, and C. H. Chan, "Circularly polarized patch antenna for future 5g mobile phones," *IEEE Access*, vol. 2, pp. 1521–1529, 2014.

[38] H. I. Cantu and V. F. Fusco, "A 21 ghz reflection amplifier mmic for retro-directive antenna and rfid applications," in *2006 IET Seminar on MM-Wave Products and Technologies*, 2006, pp. 66–70.

[39] F. Amato, C. W. Peterson, B. P. Degnan, and G. D. Durgin, "A 45 w bias power, 34 db gain reflection amplifier exploiting the tunneling effect for rfid applications," in *2015 IEEE International Conference on RFID (RFID)*, 2015, pp. 137–144.

[40] S. Khaledian, F. Farzami, B. Smida, and D. Erricolo, "Two-way backscatter communication tag using a reflection amplifier," *IEEE Microwave and Wireless Components Letters*, vol. 29, no. 6, pp. 421–423, 2019.

[41] J. Kimionis, A. Georgiadis, A. Collado, and M. M. Tentzeris, "Enhancement of rf tag backscatter efficiency with low-power reflection amplifiers," *IEEE Transactions on Microwave Theory and Techniques*, vol. 62, no. 12, pp. 3562–3571, 2014.

[42] N. Landsberg and E. Socher, "An f-band reflection amplifier using 28 nm cmos fd-soi technology for active reflectarrays and spatial power combining applications," in *2016 IEEE MTT-S International Microwave Symposium (IMS)*, 2016, pp. 1–3.

[43] A. Strobel, C. Carlowitz, R. Wolf, F. Ellinger, and M. Vossiek, "A millimeter-wave low-power active backscatter tag for fmcw radar systems," *IEEE Transactions on Microwave Theory and Techniques*, vol. 61, no. 5, pp. 1964–1972, 2013.

[44] F. Farzami, S. Khaledian, B. Smida, and D. Erricolo, "Reconfigurable dual-band bidirectional reflection amplifier with applications in van atta array," *IEEE Transactions on Microwave Theory and Techniques*, vol. 65, no. 11, pp. 4198–4207, 2017.

[45] J. Kimionis, M. M. Tentzeris, A. Georgiadis, and A. Collado, "Inkjet-printed reflection amplifier for increased-range backscatter radio," in *2014 44th European Microwave Conference*, 2014, pp. 5–8.

[46] W. L. Stutzman and G. A. Thiele, *Antenna Theory and Design*. John Wiley and Sons, Inc., 2012.

[47] D. R. Smith, V. R. Gowda, O. Yurduseven, S. Larouche, G. Lipworth, Y. Urzhumov, and M. S. Reynolds, "An analysis of beamed wireless power transfer in the fresnel zone using a dynamic, metasurface aperture," *Journal of Applied Physics*, vol. 121, no. 1, p. 014 901, 2017. eprint: https://doi.org/10.1063/1.4973345.

[48] J. W. Goodman, *Introduction to Fourier Optics*. Roberts and Company Publishers, 2005.

[49] S. Costanzo and F. Venneri, "Miniaturized fractal reflectarray element using fixed-size patch," *IEEE Antennas and Wireless Propagation Letters*, vol. 13, pp. 1437–1440, 2014.

[50] J. Jeong and D. Jang, "Design technique for harmonic-tuned rf power oscillators for high-efficiency operation," *IEEE Transactions on Industrial Electronics*, vol. 62, no. 1, pp. 221–228, 2015.

[51] Y. Yi and J. Jeong, "C-band high power and high efficiency harmonic-tuned oscillator," *Microwave and Optical Technology Letters*, vol. 58, no. 9, pp. 2281–2285, 2016. eprint: https://onlinelibrary.wiley.com/doi/pdf/10.1002/mop.30025.

[52] P.-H. Wu and S.-Y. Chen, "Design of beam-steerable dual-beam reflectarray," in *2017 IEEE International Symposium on Antennas and Propagation USNC/URSI National Radio Science Meeting*, 2017, pp. 2081–2082.

[53] O. Kiris, K. Topalli, and M. Unlu, "A reflectarray antenna using hexagonal lattice with enhanced beam steering capability," *IEEE Access*, vol. 7, pp. 45 526–45 532, 2019.

[54] E. Carrasco, M. Barba, and J. A. Encinar, "X-band reflectarray antenna with switching-beam using pin diodes and gathered elements," *IEEE Transactions on Antennas and Propagation*, vol. 60, no. 12, pp. 5700–5708, 2012.

[55] O. Bayraktar, O. A. Civi, and T. Akin, "Beam switching reflectarray monolithically integrated with rf mems switches," *IEEE Transactions on Antennas and Propagation*, vol. 60, no. 2, pp. 854–862, 2012.

[56] G.-B. Wu, S.-W. Qu, and S. Yang, "Wide-angle beam-scanning reflectarray with mechanical steering," *IEEE Transactions on Antennas and Propagation*, vol. 66, no. 1, pp. 172–181, 2018.

[57] P. Nayeri, F. Yang, and A. Z. Elsherbeni, "Bifocal design and aperture phase optimizations of reflectarray antennas for wide-angle beam scanning performance," *IEEE Transactions on Antennas and Propagation*, vol. 61, no. 9, pp. 4588–4597, 2013.

[58] H. Yi, S.-W. Qu, K.-B. Ng, C. H. Chan, and X. Bai, "3-d printed millimeter-wave and terahertz lenses with fixed and frequency scanned beam," *IEEE Transactions on Antennas and Propagation*, vol. 64, no. 2, pp. 442–449, 2016.

[59] S. Aldhaher, P. D. Mitcheson, J. M. Arteaga, G. Kkelis, and D. C. Yates, "Light-weight wireless power transfer for mid-air charging of drones," in *2017 11th European Conference on Antennas and Propagation (EUCAP)*, 2017, pp. 336–340.

[60] C. R. Valenta and G. D. Durgin, "Harvesting wireless power: Survey of energy-harvester conversion efficiency in far-field, wireless power transfer systems," *IEEE Microwave Magazine*, vol. 15, no. 4, pp. 108–120, 2014.